

Spectral Hierarchy of the Cosmic Web

Francisco-Shu Kitaura^{1,2} and Francesco Sinigaglia^{3,4,5,6,1,2}

¹Instituto de Astrofísica de Canarias, s/n, E-38205, La Laguna, Tenerife, Spain

²Departamento de Astrofísica, Universidad de La Laguna, E-38206, La Laguna, Tenerife, Spain

³Institute for Fundamental Physics of the Universe, Via Beirut 2, I-34151 Trieste, Italy

⁴SISSA - International School for Advanced Studies, Via Bonomea 265, 34136 Trieste, Italy

⁵INAF - Osservatorio Astronomico di Trieste, Via G. B. Tiepolo 11, I-34131 Trieste, Italy

⁶INFN – National Institute for Nuclear Physics, Via Valerio 2, I-34127 Trieste, Italy

E-mail: fkitauro@iac.es

Abstract. We introduce a spectral hierarchy of cosmic-web classifications obtained by applying simple scale-weighting kernels to the density field before performing a standard eigenvalue-based web classification. This unifies and extends several widely used web definitions within a single framework: the familiar potential/tidal web (large-scale, nonlocal), a curvature-based web (more local, peak- and ridge-sensitive), and additional higher-derivative levels that progressively emphasize smaller-scale structure. Because the classification is built from second derivatives of the filtered field, successive hierarchy levels align naturally with operator families that appear in renormalised bias and effective descriptions of large-scale structure, providing an explicit bridge between cosmic-web environments and long- and short-range nonlocal bias ingredients.

We quantify the information content of the hierarchy with a compact statistic: we map each cell to one of four ordered web types (void, sheet, filament, knot), construct a corresponding “web contrast” field, and measure its cross-correlation with halos from the ABACUSUMMIT simulation suite on a coarse mesh with $\Delta L \simeq 5.5 h^{-1} \text{Mpc}$. We find that the hierarchy retains significant tracer-relevant information from very large scales down to the mesh Nyquist limit, with the more local (curvature/higher-derivative) levels dominating toward nonlinear scales. This makes the spectral hierarchy a practical, interpretable conditioning basis for fast mock-galaxy production and field-level modelling, and a flexible tool for studying environment-dependent clustering and assembly bias.

Contents

1	Introduction	2
2	The cosmic web framework and generalized kernel hierarchy	2
2.1	Lagrangian–Eulerian mapping and the role of second derivatives	3
2.2	Spectral kernel hierarchy	4
3	Physical interpretation of hierarchy levels	5
3.1	$i = -4$: relativistic/gauge-screening sensitivity	5
3.2	$i = -2$: Newtonian gravitational potential	6
3.3	$i = 0$: curvature web and short-range nonlocal bias	7
3.4	$i = +2$: second higher-derivative level	8
3.5	$i = +4$: third higher-derivative level	8
3.6	$i = +2$ and $i = +4$: connection to cosmological physics	8
4	Effective Euler equation and late-time scale-dependent growth	10
4.1	From the effective Euler equation to a modified growth equation	11
4.2	Early-time behaviour and late-time activation	11
4.3	Physical interpretation	12
5	Cosmic web classification and its relation to nonlocal bias	12
5.1	Tidal tensor invariants and long-range nonlocal bias	12
5.2	Short-range nonlocality and curvature / density-derivative tensors	13
5.3	Why hierarchy helps: positive definite bias modelling via catalogue subdivision	14
6	Simulation Data	14
6.1	High-resolution particle-mesh simulation	14
6.2	ABACUS dark matter and halo catalogues	15
7	Method: web classification, information-theoretic compression, and cross-correlation	15
7.1	Generalized eigenvalue web classification at level i	16
8	Results: evidence for information in the hierarchy	17
8.1	Visual impression of hierarchical information	17
8.2	Cross power spectrum analysis	17
8.2.1	High-resolution matter field.	17
8.2.2	Halo field on coarse meshes.	18
8.3	PDF characterization and tracer footprint	18
8.4	Implications for fast mock generation	19
9	Discussion and conclusions	19

1 Introduction

The cosmic web — the network of voids, sheets, filaments and knots — is a defining feature of the late-time Universe [e.g., 1–3]. It encodes anisotropic gravitational collapse and provides a natural language for describing environment-dependent phenomena, including galaxy formation pathways and assembly bias. Cosmic web information is exploited across a broad range of applications: missing baryons in filaments, void cosmology, redshift-space distortions, dark energy constraints, and tests of gravity [e.g., 4–7]. A long-standing challenge is that “cosmic web” remains method-dependent; different classifiers emphasize different aspects of the field [3].

In parallel, modern large-scale structure analysis increasingly relies on forward models and fast mock catalogues. Accurate mock generation for current and upcoming surveys requires an efficient yet physically grounded representation of tracer bias, including nonlocality and stochasticity. Effective field-level bias models have matured significantly [8, 9], and a key insight is that nonlocal bias operators are closely related to tidal and curvature information in the underlying density field. A particularly powerful approach is the hierarchical cosmic web assembly-bias framework, which treats different cosmic web regions as distinct tracer subsets and thereby captures long- and short-range nonlocality indirectly [10, 11].

In this work we extend the concept of cosmic web classification by introducing a spectral hierarchy defined by kernel operators acting on the density contrast in Fourier space. This hierarchy: (i) unifies standard potential-based and curvature-based web definitions as particular levels, (ii) naturally connects to long- and short-range nonlocal bias operators, (iii) offers additional levels motivated by higher-derivative bias and effective field theory, and (iv) yields a compact information-theoretic compression of environment that demonstrably correlates with halo catalogues down to mesh Nyquist scales relevant for fast mock generation.

The present work is also a companion paper to a series of studies that use the **WebOn** framework—most notably its spectral hierarchical cosmic-web classification—as a core ingredient for field-level bias modelling and subgrid tracer placement [e.g. 11, 12].

2 The cosmic web framework and generalized kernel hierarchy

In this section we recap the foundations of cosmic web classification and explain why it provides a natural language to design scale-separated and hierarchical operators for large-scale structure analyses and fast forward modelling. The cosmic web is the emergent anisotropic pattern of knots, filaments, sheets and voids produced by gravitational instability. A broad class of cosmic web classifiers can be understood as diagnostics of second derivatives of either the gravitational potential or the density field, i.e. of the local curvature of the evolved large-scale structure.

Standard (tidal) cosmic web approaches are based on the tidal tensor,

$$T_{ij}(\mathbf{x}) \equiv \partial_i \partial_j \phi(\mathbf{x}), \quad (2.1)$$

where ϕ is the (dimensionless) peculiar gravitational potential obeying $\nabla^2 \phi(\mathbf{x}) = \delta(\mathbf{x})$. The eigenvalues of T_{ij} quantify collapse/expansion along principal directions, motivating the classification of the environment into four morphological components (knots, filaments, sheets and voids) according to the number of eigenvalues above a threshold.

This construction is rooted in the local equations of motion. For a test particle in comoving coordinates, the peculiar gravitational acceleration is

$$\ddot{x}_i = -\partial_i \phi(\mathbf{x}), \quad (2.2)$$

where dots denote derivatives with respect to time. Expanding the force to first order around a reference position $\bar{\mathbf{x}}$ gives the linearized equation for the separation $\Delta x_i \equiv x_i - \bar{x}_i$ of neighbouring fluid elements,

$$\Delta \ddot{x}_i = -\sum_j \partial_i \partial_j \phi|_{\bar{\mathbf{x}}} \Delta x_j = -\sum_j T_{ij}(\bar{\mathbf{x}}) \Delta x_j. \quad (2.3)$$

Thus the tidal tensor governs the relative acceleration along the principal axes of the flow. After diagonalization, Eq. (2.3) reduces locally to three independent equations,

$$\Delta \ddot{x}_i = -\lambda_i \Delta x_i, \quad (2.4)$$

where λ_i are the eigenvalues of T_{ij} . Their signs determine whether neighbouring trajectories converge or diverge along each principal direction, providing the dynamical basis for classifying regions into knots, filaments, sheets, and voids, as emphasized in Hahn et al. 2007 [13].

While the tidal tensor provides the most direct dynamical description of anisotropic collapse, it is only one particular realization of a broader second-derivative perspective on the cosmic web. A closely related and more local construction is obtained by acting directly on the evolved density field rather than on the gravitational potential. This leads to classifiers built from the Hessian of the density,

$$H_{ij}(\mathbf{x}) \equiv \partial_i \partial_j \delta(\mathbf{x}), \quad (2.5)$$

which are more sensitive to short-range curvature and peak-like structure, and therefore provide a complementary handle on the small-scale geometry of the web. The tidal tensor and the density Hessian can thus be regarded as adjacent members of a wider family of anisotropy diagnostics: the former probes non-local, potential-driven structure formation, whereas the latter probes the local curvature of the matter field itself. In both cases, the eigenvalues and rotational invariants capture anisotropic information beyond the local density and provide a natural bridge between cosmic-web morphology and operator-based descriptions of large-scale structure.

Motivated by this, we introduce the notion of a generalized kernel hierarchy: a family of kernels defining progressively different degrees of nonlocality and derivative order that can be applied either (i) as classifiers (discrete web labels) or (ii) as continuous fields (filtered curvature and ridge measures), with the goal of organizing information content across scales in a controlled and computationally efficient way. In particular, by arranging operators in a spectral ladder, we can interpret web information as a compact summary of the field content that enters bias expansions and effective stress-tensor descriptions.

2.1 Lagrangian–Eulerian mapping and the role of second derivatives

The Lagrangian–Eulerian mapping,

$$\mathbf{x}(\mathbf{q}, z) = \mathbf{q} + \Psi(\mathbf{q}, z), \quad (2.6)$$

encodes structure formation through the displacement field Ψ . The Eulerian density contrast can be written in terms of the Jacobian of this mapping,

$$1 + \delta(\mathbf{x}) = \sum_{\mathbf{q}_*} \left| \det \left(\delta_{ij}^K + \frac{\partial \Psi_i}{\partial q_j} \right) \right|_{\mathbf{q}_*}^{-1}, \quad (2.7)$$

where the sum runs over all streams \mathbf{q}_* mapping to the same Eulerian position. Before shell crossing, the mapping is single-valued and local collapse is controlled by the eigenvalues of the deformation tensor $\partial \Psi_i / \partial q_j$. After shell crossing, multi-streaming appears and the density field develops sharp anisotropic features (ridges).

Second derivatives enter naturally at two connected levels:

(i) Large-scale anisotropic transport. In perturbation theory, the displacement is potential, $\Psi = -\nabla\Phi$, so the deformation tensor is a Hessian. In the Zel'dovich approximation and its higher-order extensions, tidal effects are therefore captured by second derivatives of a potential, and the eigen-structure of such Hessians determines preferential collapse directions.

(ii) Eulerian curvature and ridge sharpening. Once particles have been transported to Eulerian space, the local morphology of the density field—whether matter lies in a knot, filament, sheet or void—is governed by the eigenvalues of curvature tensors such as T_{ij} and H_{ij} . Ridges correspond to directions of maximal compression and large curvature transverse to the ridge. This is the regime where higher-derivative operator content becomes increasingly relevant: it characterizes how short-range morphology reacts to coarse-graining and how additional relaxation can be parameterized in effective descriptions.

Generalized kernel hierarchy. To make this connection explicit, consider a family of kernels defining a nested set of filtered fields,

$$\delta^{(n)}(\mathbf{k}) \equiv K_n(k) \hat{\delta}(\mathbf{k}), \quad K_{n+1}(k) \leq K_n(k), \quad (2.8)$$

so that n indexes progressively shorter-range information. Gaussian kernels of the form $K_n(k) = \exp[-k^2 r_n^2 / 2]$ are a convenient choice, but other kernels can be used. One can then define hierarchical curvature tensors,

$$T_{ij}^{(n)}(\mathbf{x}) \equiv \partial_i \partial_j \phi^{(n)}(\mathbf{x}), \quad H_{ij}^{(n)}(\mathbf{x}) \equiv \partial_i \partial_j \delta^{(n)}(\mathbf{x}), \quad (2.9)$$

and their eigenvalues/invariants to obtain either discrete web labels at each level n or continuous ridge measures. The spectral hierarchy introduced below provides an analytically simple and operator-aligned version of this idea, in which the filtration is organized by integer even powers of k .

2.2 Spectral kernel hierarchy

We define a family of filtered fields via Fourier-space kernel operators

$$\hat{\delta}^{(i)}(\mathbf{k}) \equiv -k^i \hat{\delta}(\mathbf{k}), \quad i \in 2\mathbb{Z}. \quad (2.10)$$

The overall minus sign is a convention consistent with potential-based operators (e.g., $\phi \propto -\nabla^{-2}\delta$). In real space, the index i controls the degree of derivative/nonlocality:

$$\delta^{(i)}(\mathbf{x}) \propto \begin{cases} \nabla^i \delta(\mathbf{x}) & i > 0, \\ \nabla^{-|i|} \delta(\mathbf{x}) & i < 0. \end{cases} \quad (2.11)$$

For each level i , we define the generalized Hessian tensor

$$\mathcal{H}_{ab}^{(i)}(\mathbf{x}) \equiv \partial_a \partial_b \delta^{(i)}(\mathbf{x}). \quad (2.12)$$

Interestingly, the spectral hierarchy reproduces the same derivative ladder that appears in renormalized bias and EFT descriptions of large-scale structure. Because the classification tensor involves two additional derivatives of the filtered field, its scalar invariants involve operator structures scaling as $\nabla^2 \delta$, $\nabla^4 \delta$, $\nabla^6 \delta$, and higher orders, corresponding to the gradient expansion discussed in bias theory and effective field theory [8, 9, 38].

3 Physical interpretation of hierarchy levels

The generalized kernel hierarchy introduced in Sec. 2 provides a unified way of organizing gravitational evolution and effective corrections according to their derivative order. Each hierarchy level can be associated with a characteristic physical regime, ranging from relativistic large-scale effects to highly nonlinear short-range relaxation. In this section we provide a physical interpretation of the different levels in terms of scale, dynamics, and their relevance for fast forward models.

We will use a compact operator notation throughout. For even i we define

$$\mathcal{O}_i[\delta](\mathbf{k}) \equiv -k^i \hat{\delta}(\mathbf{k}), \quad i \in 2\mathbb{Z}, \quad (3.1)$$

so that $\delta^{(i)} = \mathcal{O}_i[\delta]$ and $\mathcal{H}_{ab}^{(i)} = \partial_a \partial_b \mathcal{O}_i[\delta]$. Negative indices correspond to inverse-Laplacian (long-range) operators and positive indices to increasingly local, short-range operators. Long-range levels encode coherent gravitational transport and tidal evolution, whereas higher positive levels encode local relaxation, curvature sensitivity, and small-scale stabilization. The intermediate levels correspond to the standard Newtonian regime captured by LPT and its augmented variants. A compact summary of the levels is provided in Tab. 1.

3.1 $i = -4$: relativistic/gauge-screening sensitivity

The level $i = -4$ corresponds to operators involving higher inverse powers of the Laplacian, schematically of the form

$$\mathcal{O}_{-4}[\delta] \sim \nabla^{-4} \delta. \quad (3.2)$$

Such terms are extremely long-range and sensitive to large-scale boundary conditions and gauge choices [see 14]. Physically, they can be interpreted as encoding relativistic and screening-like effects that become relevant on horizon scales.

In Newtonian gravity, the dominant long-range operator is $\nabla^{-2} \delta$, which gives rise to the Poisson equation. However, when considering relativistic corrections or effective large-scale modifications (e.g. gauge effects in cosmological perturbation theory, infrared resummations, or horizon-scale screening), higher inverse-Laplacian structures naturally appear. These operators amplify the contribution of ultra-large-scale modes and therefore control the coupling between super-horizon perturbations and sub-horizon evolution.

Relativistic corrections introduce an additional infrared contribution to the displacement field that depends on a time-dependent screening length $\ell(a)$ [14]. Using the approximation derived in that work, the shift between the conformal Newtonian (CN) gauge particle positions and the simulation comoving synchronous (CS) coordinates can be written in Fourier space as

$$\Psi_{\text{CS} \rightarrow \text{CN}}(\mathbf{k}, a) \approx \frac{i\mathbf{k}}{\ell^2(a) k^4} \delta(\mathbf{k}, a), \quad (3.3)$$

so that the divergence of the displacement correction becomes

$$\nabla \cdot \Psi_{\text{CS} \rightarrow \text{CN}} = -\frac{1}{\ell^2(a) k^4} \delta(\mathbf{k}, a). \quad (3.4)$$

The time-dependent screening length is approximately

$$\ell(a) = \ell_0 a^{2/7} \left(\frac{H}{H_0} \right)^{-3/7}, \quad \ell_0 = \frac{c}{\sqrt{3} H_0} \Omega_m^{-2/7}. \quad (3.5)$$

This expression shows that relativistic corrections introduce an additional k^{-4} contribution to the displacement divergence, naturally corresponding to the lowest level of the spectral hierarchy ($i = -4$), while the factor $\ell(a)$ provides a horizon-scale screening that suppresses the effect on sub-horizon modes [see also 15–19].

In the context of fast gravity solvers, $i = -4$ levels are typically subdominant for mock catalogue production at sub-horizon scales. Nevertheless, they provide a formal link between Newtonian operator hierarchies and relativistic perturbation theory. In particular, they highlight that the lowest hierarchy levels are sensitive to the global cosmological frame and to long-wavelength modes that modulate local structure formation (the separate-universe picture). From a practical perspective, $i = -4$ contributions may become relevant when generating very large-volume lightcones approaching horizon scales or when incorporating relativistic light-cone effects and gauge corrections.

3.2 $i = -2$: Newtonian gravitational potential

The level $i = -2$ corresponds to the standard Newtonian Poisson operator,

$$\mathcal{O}_{-2}[\delta] \sim \nabla^{-2} \delta, \quad (3.6)$$

which determines the gravitational potential through $\nabla^2 \phi \propto \delta$. This level defines the backbone of structure formation in the Newtonian regime. It encodes the long-range, non-local nature of gravity: density perturbations source a potential that extends over arbitrarily large distances. In Fourier space, the operator scales as k^{-2} , implying that large-scale modes dominate the gravitational response.

All Lagrangian Perturbation Theory (LPT) approaches—including 2LPT and ALPT—are fundamentally built upon this level. The displacement field,

$$\Psi \sim -\nabla \nabla^{-2} \delta, \quad (3.7)$$

is directly constructed from \mathcal{O}_{-2} . Thus, $i = -2$ governs coherent bulk flows, tidal transport, and large-scale anisotropic collapse, providing the correct infrared behaviour required for large-volume mock production.

The same tidal tensor that governs large-scale anisotropic collapse also plays a central role in tidal torque theory (TTT), which explains the origin of angular momentum in proto-haloes [24–29]. In this framework the angular momentum of a collapsing proto-halo is generated by the misalignment between its inertia tensor and the surrounding tidal field $T_{ij} = \partial_i \partial_j \phi$. At leading order the torque scales schematically as

$$L_i \propto \epsilon_{ijk} I_{jl} T_{lk}, \quad (3.8)$$

where I_{ij} is the inertia tensor of the proto-halo region. Since the tidal tensor corresponds precisely to the $i = -2$ level of the spectral hierarchy, this level also encodes the large-scale tidal environment responsible for generating halo angular momentum. In this sense, the potential-based cosmic web classification naturally captures the large-scale dynamical structures that influence both anisotropic collapse and the spin acquisition of dark matter haloes.

Primordial non-Gaussianity (PNG) provides another example of physically relevant scale-dependent structure on the infrared side of the hierarchy. In particular, local-type PNG induces the well-known large-scale scale-dependent halo-bias correction

$$\Delta b(k) \propto f_{\text{NL}} k^{-2}, \quad (3.9)$$

which is associated with the primordial-potential operator and therefore maps naturally onto the potential-dominated $i = -2$ level of the spectral hierarchy, rather than onto the more infrared $i = -4$ level [9, 33]. PNG is commonly parameterized through the dimensionless coefficient f_{NL} by writing the primordial Bardeen potential as

$$\Phi(\mathbf{q}) = \phi(\mathbf{q}) + f_{\text{NL}} [\phi^2(\mathbf{q}) - \langle \phi^2 \rangle], \quad (3.10)$$

where ϕ is a Gaussian random field in Lagrangian coordinates \mathbf{q} [17, 21–23, 33, for relevant studies].

The PNG signal therefore traces the same k^{-2} potential operator that governs Newtonian tidal dynamics. Here the hierarchy label refers to the filtered scalar field itself, not to the derivative order of the Hessian invariants used in the classifier. It is important to distinguish between the hierarchy level of the filtered scalar field and the effective operator appearing in the scalar invariants of the classifier.

Since the Hessian introduces two additional derivatives, a field filtered as $k^i \delta$ produces a trace scaling as $k^{i+2} \delta$. Thus, the standard tidal web ($i = -2$) has trace $\propto \delta$, a classifier whose trace scales as $k^{-2} \delta$ would correspond to $i = -4$, and one whose trace scales as $k^{-4} \delta$ would correspond to $i = -6$. This implies that GR screening might be studied with $i = -6$ and PNG with $i = -4$ (!).

3.3 $i = 0$: curvature web and short-range nonlocal bias

The level $i = 0$ corresponds to the operator:

$$\mathcal{O}_0[\delta] \sim -\delta, \quad (3.11)$$

and

$$\mathcal{H}_{ij}^{(0)} = -\partial_i \partial_j \delta. \quad (3.12)$$

In Fourier space this tensor scales as $k_i k_j \delta(\mathbf{k})$, so its trace corresponds to

$$\text{Tr } \mathcal{H}^{(0)} \propto \nabla^2 \delta. \quad (3.13)$$

Thus the $i = 0$ level is directly connected to the leading higher-derivative bias operator $\nabla^2 \delta$ discussed in peak theory [30, 31] and renormalized bias theory [e.g., 8, 9]. Physically, this operator encodes finite Lagrangian size and formation-scale sensitivity of tracers. It represents the first short-range nonlocal correction beyond density and tidal invariants.

In geometric terms, $i = 0$ defines a curvature web: regions are classified according to the Hessian of the density field, emphasizing peaks, ridges and saddle morphology [27, 32].

3.4 $i = +2$: second higher-derivative level

For $i = 2$ one obtains

$$\delta^{(2)}(\mathbf{k}) = -k^2 \delta(\mathbf{k}), \quad (3.14)$$

so that in real space (up to the overall sign convention)

$$\mathcal{O}_2[\delta] \sim \delta^{(2)}(\mathbf{x}) \propto \nabla^2 \delta(\mathbf{x}). \quad (3.15)$$

The generalized classification tensor is

$$\mathcal{H}_{ij}^{(2)} \equiv \partial_i \partial_j \delta^{(2)}(\mathbf{x}) \iff \mathcal{H}_{ij}^{(2)}(\mathbf{k}) \propto k_i k_j k^2 \delta(\mathbf{k}). \quad (3.16)$$

Accordingly, the leading rotationally invariant scalar built from the classification tensor (its trace) scales as

$$\text{Tr } \mathcal{H}^{(2)} = \nabla^2 \delta^{(2)} \propto \nabla^4 \delta. \quad (3.17)$$

Such operators appear naturally as subleading higher-derivative terms in bias expansions and as next-order gradient corrections in effective field theory descriptions of large-scale structure. Physically, they encode sensitivity to curvature gradients and to increasingly localized morphological structure. Their contribution becomes relevant toward smaller scales where finite-size and coarse-graining effects are more pronounced.

3.5 $i = +4$: third higher-derivative level

For $i = 4$ one has

$$\delta^{(4)}(\mathbf{k}) = -k^4 \delta(\mathbf{k}), \quad (3.18)$$

so that in real space (again up to the overall sign convention)

$$\mathcal{O}_4[\delta] \sim \delta^{(4)}(\mathbf{x}) \propto \nabla^4 \delta(\mathbf{x}). \quad (3.19)$$

The corresponding classification tensor satisfies

$$\mathcal{H}_{ij}^{(4)}(\mathbf{k}) \propto k_i k_j k^4 \delta(\mathbf{k}), \quad (3.20)$$

and its trace scales as

$$\text{Tr } \mathcal{H}^{(4)} = \nabla^2 \delta^{(4)} \propto \nabla^6 \delta. \quad (3.21)$$

Operators of this type arise as higher-order UV-sensitive terms in renormalized bias theory and in effective field theory treatments, where successive gradient corrections encode increasingly short-range response. While typically suppressed at large scales, they become relevant near the ultraviolet cutoff of a numerical mesh or in highly nonlinear environments.

3.6 $i = +2$ and $i = +4$: connection to cosmological physics

Scale-dependent operators similar to those appearing in the ultraviolet levels of the spectral hierarchy also arise in cosmological models with additional particle species or modified dark-matter dynamics. From the perspective of the spectral hierarchy, such behaviour can be viewed as motivating effective scale-dependent responses that, in an appropriate gradient expansion, are analogous to the operator structures associated with the $i = 0$ and $i = 2$ levels. In the linear regime this effect can be described through a modified growth response that depends on k^2/k_{fs}^2 relative to the neutrino free-streaming scale k_{fs} [37].

Level i	Field $\delta^{(i)}(\mathbf{k})$	Physical interpretation / operator content
-4	$-k^{-4} \hat{\delta}(\mathbf{k})$	IR-enhanced relativistic/gauge-screening level. Real-space $\delta^{(-4)} \propto -\nabla^{-4}\delta$. Connects to conformal Newtonian gauge GR-screening/displacement-like corrections; emphasizes ultra-large-scale morphology [14–19].
-2	$-k^{-2} \hat{\delta}(\mathbf{k})$	Potential / tidal-tensor level (classical T-web). $\delta^{(-2)} \propto \phi$ with $\nabla^2\phi = \delta$ and $\mathcal{H}_{ij}^{(-2)} = \partial_i\partial_j\phi$. Encodes anisotropic collapse and long-range tidal environments; relates to long-range nonlocal bias through tidal invariants (e.g., s^2, s^3) [25, 27–29, 34–36] and to large-scale scale-dependent bias from primordial non-Gaussianity [21–23, 33].
0	$-k^0 \hat{\delta}(\mathbf{k})$	Curvature level (density Hessian). $\delta^{(0)} = -\delta$ and $\mathcal{H}_{ij}^{(0)} = -\partial_i\partial_j\delta$. The trace gives $\text{Tr } \mathcal{H}^{(0)} \propto \nabla^2\delta$. Highlights curvature/peak morphology; connects to tidal-torque ingredients and short-range conditioning used in bias models [8, 9, 11, 27].
2	$-k^2 \hat{\delta}(\mathbf{k})$	Next higher-derivative level. $\delta^{(2)} \propto \nabla^2\delta$, but the web classifier uses a Hessian, so its scalar invariants carry two additional derivatives; in particular $\text{Tr } \mathcal{H}^{(2)} \propto \nabla^4\delta$. This is the next derivative order in the invariants, and it becomes relevant toward the UV/mesh cutoff. Related to higher-derivative bias and EFT operator expansions; can also provide an effective language for scale-dependent responses arising from massive neutrinos, non-standard dark matter, or modified-gravity models. [9, 37–43].
4	$-k^4 \hat{\delta}(\mathbf{k})$	Higher-derivative level (UV-sensitive). $\delta^{(4)} \propto \nabla^4\delta$; correspondingly $\text{Tr } \mathcal{H}^{(4)} \propto \nabla^6\delta$. Represents the subsequent gradient order in the invariants and is typically the most UV-sensitive level. Related to higher-derivative bias and EFT operator expansions; can also provide an effective language for scale-dependent responses arising from massive neutrinos, non-standard dark matter, or modified-gravity models. [9, 37–43].

Table 1. Spectral hierarchy levels for the kernel ladder $\delta^{(i)}(\mathbf{k}) \equiv -k^i \hat{\delta}(\mathbf{k})$ (even i). Each level corresponds to a distinct degree of nonlocality/derivative order and aligns with operator sectors used in renormalised bias and EFT descriptions.

From the perspective of the spectral hierarchy, such behaviour corresponds to a response that depends on higher spatial derivatives of the density field, analogous to the operators associated with the $i = 0$ and $i = 2$ levels.

Similarly, several dark-matter models introduce characteristic scale-dependent corrections to the effective gravitational response. Examples include warm dark matter, fuzzy/ultralight dark matter [44], and effective fluid descriptions of small-scale dark matter dynamics [38–41] and bias expansions [9]. These models typically produce gradient terms in the effective Euler equation or modified Poisson relations involving operators such as $\nabla^2\delta$ or $\nabla^4\delta$. Such terms correspond naturally to the higher rungs ($i = 2, 4$) of the spectral hierarchy and therefore provide a physical interpretation of these levels in terms of short-range dynamical corrections. While the present work does not attempt to model these effects explicitly, the hierarchy provides a convenient language for organizing and potentially detecting scale-dependent signatures associated with neutrino free-streaming or non-standard dark-matter physics [see 45].

A useful complementary perspective on the ultraviolet rungs of the hierarchy is also provided by modified-gravity. In $f(R)$ gravity the gravitational action is modified by replacing the Ricci scalar R with a function $f(R)$, so that cosmic acceleration can arise from modified spacetime geometry rather than from a cosmological constant. For example, in the quasistatic limit of $f(R)$ gravity the effective gravitational constant becomes scale dependent and takes the form

$$G_{\text{eff}}(k, a) = \frac{1}{8\pi F} \frac{1 + 4m k^2/(a^2 R)}{1 + 3m k^2/(a^2 R)}, \quad (3.22)$$

where $F \equiv \partial f/\partial R$ and

$$m \equiv \frac{d \ln F}{d \ln R} \quad (3.23)$$

controls the scale dependence of the modified response [42, 43]. Expanding in the small parameter

$$x \equiv \frac{m k^2}{a^2 R} \ll 1 \quad (3.24)$$

yields

$$\frac{1 + 4x}{1 + 3x} = 1 + x - 3x^2 + 9x^3 + \dots \quad (3.25)$$

The modified Poisson equation can then be written schematically in configuration space as

$$\nabla^2 \Phi = 4\pi G a^2 \bar{\rho}_m \frac{1}{F} \left[\delta - \frac{m}{a^2 R} \nabla^2 \delta - \frac{3m^2}{(a^2 R)^2} \nabla^4 \delta - \frac{9m^3}{(a^2 R)^3} \nabla^6 \delta + \dots \right]. \quad (3.26)$$

This makes explicit that higher-derivative operators such as $\nabla^2 \delta$, $\nabla^4 \delta$ and $\nabla^6 \delta$ arise naturally in a controlled expansion of the scale-dependent gravitational response. A closely related logic appears in EFT-based descriptions of large-scale structure, where successive higher-derivative terms encode the effect of unresolved short-scale physics and finite-size response.

4 Effective Euler equation and late-time scale-dependent growth

In two-step or relaxation-augmented gravity solvers, the short-range step can be interpreted as an additional effective contribution to the matter Euler equation beyond pressureless dust. At the field level, such corrections arise from coarse-graining unresolved small-scale dynamics and can be organised as a gradient expansion of an effective stress tensor in powers of spatial derivatives of the density contrast. To leading order, this produces operators of the form $\nabla^2 \delta$ and $\nabla^4 \delta$.

These operators do not represent primordial modifications of gravity. Rather, they encode late-time, small-scale response effects associated with halo relaxation, virialisation, and unresolved nonlinear collapse. In the context of the spectral hierarchy, they provide a continuous description of the ultraviolet levels ($i = 2, 4$) as controlled, scale-dependent modifications of growth. Higher-order tensors such as $\partial_i \partial_j \nabla^2 \delta$ and $\partial_i \partial_j \nabla^4 \delta$ naturally arise in derivative expansions of tracer bias and in effective field theory descriptions of coarse-grained large-scale structure. They encode finite-size and curvature-gradient response of tracers and become increasingly relevant toward the nonlinear and ultraviolet regime.

4.1 From the effective Euler equation to a modified growth equation

We begin with the standard continuity–Euler–Poisson system in conformal time τ :

$$\delta' + \nabla \cdot [(1 + \delta)\mathbf{v}] = 0, \quad (4.1)$$

$$\mathbf{v}' + \mathcal{H}\mathbf{v} + (\mathbf{v} \cdot \nabla)\mathbf{v} = -\nabla\phi + \mathbf{a}_{\text{eff}}, \quad (4.2)$$

$$\nabla^2\phi = \frac{3}{2}\mathcal{H}^2\Omega_m(\tau)\delta, \quad (4.3)$$

where $\mathcal{H} = a'/a$ is the conformal Hubble rate and a prime denotes $d/d\tau$.

A lowest-order gradient expansion consistent with isotropy allows

$$\mathbf{a}_{\text{eff}} = -\frac{c_2^2(\tau)}{a^2}\nabla\delta + \frac{c_4^2(\tau)}{a^4}\nabla\nabla^2\delta + \dots, \quad (4.4)$$

where c_2 and c_4 are effective coefficients encoding short-range response.

Linearising the system and defining $\theta \equiv \nabla \cdot \mathbf{v}$, the divergence of the Euler equation yields in configuration space:

$$\theta'(\mathbf{x}) + \mathcal{H}\theta(\mathbf{x}) = -\frac{3}{2}\mathcal{H}^2\Omega_m(\tau)\delta(\mathbf{x}) - \frac{c_2^2(\tau)}{a^2}\nabla^2\delta(\mathbf{x}) + \frac{c_4^2(\tau)}{a^4}\nabla^4\delta(\mathbf{x}), \quad (4.5)$$

where $\theta \equiv \nabla \cdot \mathbf{v}$ and $\nabla^4 \equiv (\nabla^2)^2$.

In Fourier space, the same relation reads:

$$\theta' + \mathcal{H}\theta = -\frac{3}{2}\mathcal{H}^2\Omega_m\delta + \frac{c_2^2}{a^2}k^2\delta + \frac{c_4^2}{a^4}k^4\delta. \quad (4.6)$$

Using the linear continuity equation $\delta' = -\theta$, one obtains the second-order equation

$$\delta'' + \mathcal{H}\delta' - \frac{3}{2}\mathcal{H}^2\Omega_m\delta + \frac{c_2^2}{a^2}k^2\delta + \frac{c_4^2}{a^4}k^4\delta = 0. \quad (4.7)$$

Expressing the evolution in terms of derivatives with respect to $\ln a$ (dots), and using $\mathcal{H} = aH$, we obtain

$$\ddot{D} + \left(2 + \frac{d \ln H}{d \ln a}\right)\dot{D} - \frac{3}{2}\Omega_m(a)D + \frac{c_2^2(a)}{a^2 H^2(a)}k^2 D + \frac{c_4^2(a)}{a^4 H^2(a)}k^4 D = 0. \quad (4.8)$$

4.2 Early-time behaviour and late-time activation

Equation (4.8) captures the effect of short-range gradient operators. However, if the coefficients c_2 and c_4 are taken to be constant, the k^4 term scales as $\propto 1/a$ during matter domination, which would incorrectly dominate at very early times. This behaviour is unphysical in our context, since the effective operators are intended to model late-time nonlinear relaxation rather than primordial dynamics.

To enforce the intended interpretation, we introduce a smooth late-time activation function

$$S(a) = \frac{1}{2} \left[1 + \tanh \left(\frac{\ln(a/a_*)}{\Delta} \right) \right], \quad (4.9)$$

which ensures that the UV corrections switch on only once nonlinear collapse becomes significant. We further absorb the explicit $a^{-2}H^{-2}$ and $a^{-4}H^{-2}$ factors into dimensionless response functions $\beta_2(a)$ and $\beta_4(a)$, yielding the phenomenological growth equation

$$\ddot{D} + \left(2 + \frac{d \ln H}{d \ln a}\right)\dot{D} - \frac{3}{2}\Omega_m(a)D + S(a) \left[\beta_2(a) \left(\frac{k}{k_{\text{ref}}} \right)^2 + \beta_4(a) \left(\frac{k}{k_{\text{ref}}} \right)^4 \right] D = 0. \quad (4.10)$$

Here k_{ref} denotes a reference scale, typically chosen near the mesh Nyquist frequency.

Figure 1 shows numerical solutions of Eq. (4.10) for representative wavenumbers, demonstrating that the UV response remains negligible at early times ($a \ll a_\star \sim 3 \times 10^{-2}$) and becomes increasingly important toward late times, with stronger deviations at larger k .

4.3 Physical interpretation

Equation (4.10) provides a controlled, late-time, scale-dependent modification of the growth rate. For $\beta_n > 0$, high- k growth is suppressed, mimicking effective stress or coarse-grained pressure-like regularisation. For $\beta_n < 0$, high- k growth is enhanced, which can phenomenologically describe additional short-range collapse associated with relaxation-type updates.

Because $S(a) \rightarrow 0$ at early times, the evolution asymptotically reduces to the standard dust growth equation for $a \ll a_\star$. In numerical solutions, a small constant offset between the modified and dust growth factors may be observed at early times. This reflects the chosen normalization of $D(a)$ (e.g. enforcing $D(a = 1) = 1$), rather than a physical modification of early-time dynamics. The shape of the growing mode remains consistent with dust evolution in the limit $a \rightarrow 0$, and no unphysical early-time dominance or instability is introduced.

In particular, the early-time solutions remain within the growing-mode subspace of the dust equation, differing only by an overall multiplicative factor that is absorbed by late-time normalization.

5 Cosmic web classification and its relation to nonlocal bias

A central motivation for this work is that cosmic web classification is not merely a morphological descriptor: it encodes the same tensor invariants that appear in long-range nonlocal bias expansions. This insight was developed explicitly in hierarchical cosmic web assembly-bias approaches [10, 11]. Here we summarize and generalize that connection, and show how the spectral hierarchy provides a systematic extension.

This section is a conceptual interpretation that motivates the UV levels; the hierarchy itself is defined purely by the spectral operators.

5.1 Tidal tensor invariants and long-range nonlocal bias

Consider the tidal tensor $\mathcal{T}_{ij} = \partial_i \partial_j \phi$ and its eigenvalues $\lambda_1 \geq \lambda_2 \geq \lambda_3$. Define the invariants

$$I_1 = \lambda_1 + \lambda_2 + \lambda_3, \quad I_2 = \lambda_1 \lambda_2 + \lambda_1 \lambda_3 + \lambda_2 \lambda_3, \quad I_3 = \lambda_1 \lambda_2 \lambda_3. \quad (5.1)$$

For $\nabla^2 \phi = \delta$, one has $I_1 = \delta$. Writing the traceless tidal tensor

$$s_{ij} \equiv \mathcal{T}_{ij} - \frac{1}{3} \delta_{ij}^K \delta, \quad (5.2)$$

the scalar nonlocal operators in bias expansions can be expressed in terms of invariants, e.g.

$$\delta = I_1, \quad s^2 \equiv s_{ij} s_{ji} = \frac{2}{3} I_1^2 - 2 I_2, \quad s^3 \equiv s_{ij} s_{jk} s_{ki} = -I_1 I_2 + 3 I_3 + \frac{2}{9} I_1^3. \quad (5.3)$$

Thus, any classification that segments space by the signs and relative magnitudes of $(\lambda_1, \lambda_2, \lambda_3)$ implicitly conditions on (I_1, I_2, I_3) and therefore on (δ, s^2, s^3) . This explains why the $i = -2$ level can encode long-range nonlocal bias information without explicitly inserting nonlocal operators into a bias model [10, 11].

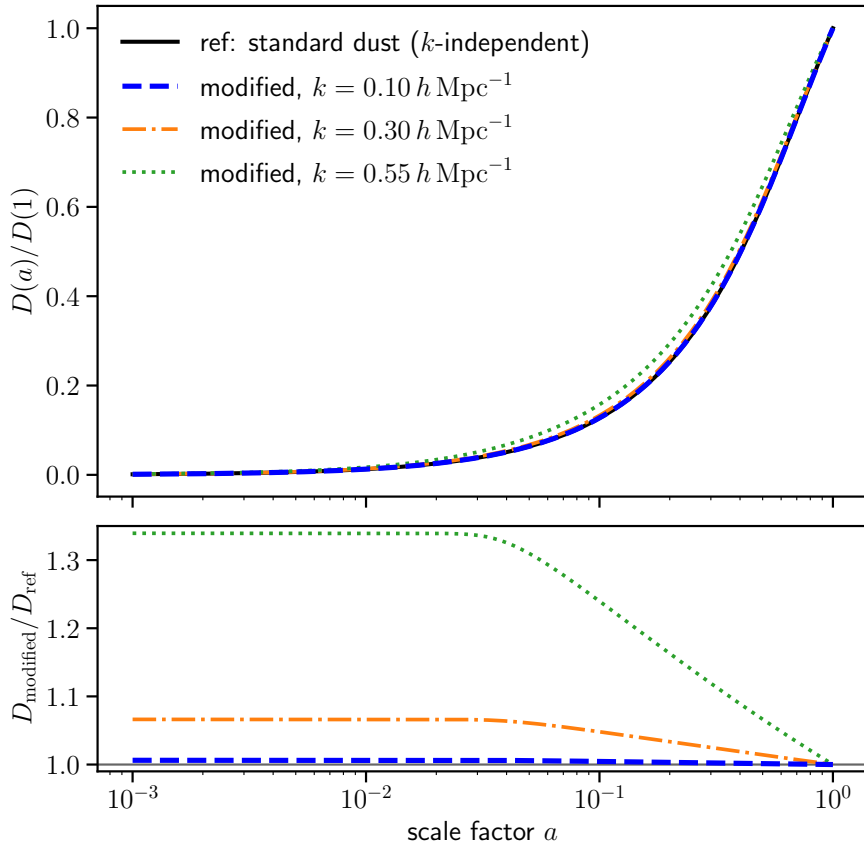


Figure 1. Scale-dependent growth with late-time UV activation. **Top panel:** Linear growth factor $D(a)$ obtained by solving Eq. (4.10) for a flat Λ CDM background. The solid black curve shows the standard dust solution (scale independent). Dashed coloured curves include scale-dependent UV response terms proportional to $(k/k_{\text{ref}})^2$ and $(k/k_{\text{ref}})^4$, activated at late times through the smooth switching function $S(a)$ defined in Eq. (4.9). **Bottom panel:** Ratio $D_{\text{modified}}/D_{\text{ref}}$ highlighting deviations. Deviations remain negligible at early times ($a \ll a_*$), confirming that the dust growing mode is recovered prior to the onset of nonlinear clustering. At late times, high- k modes experience controlled deviations, illustrating how such corrections become relevant toward the UV limit of coarse-resolution solvers.

5.2 Short-range nonlocality and curvature / density-derivative tensors

Short-range nonlocal bias contributions can be organized via density-derivative tensors, e.g. $\Gamma_{ij} \equiv \partial_i \partial_j \delta$. Define the traceless part

$$\mu_{ij} \equiv \Gamma_{ij} - \frac{1}{3} \delta_{ij}^K \nabla^2 \delta, \quad (5.4)$$

and invariants $\mu^2 \equiv \mu_{ij} \mu_{ji}$, $\mu^3 \equiv \mu_{ij} \mu_{jk} \mu_{ki}$. In hierarchical assembly-bias approaches one can sub-classify $i = -2$ regions using curvature information, thereby conditioning on short-range operator content [11].

Within the spectral hierarchy, $i = 0$ is the natural curvature (density Hessian) level, and $i = 2, 4$ extend this idea to higher derivatives: these levels systematically correspond to higher-derivative operator families in bias expansions, offering a controlled ladder of short-range information aligned with renormalised operator content.

5.3 Why hierarchy helps: positive definite bias modelling via catalogue subdivision

A practical issue with truncated explicit bias expansions is that they can yield negative predicted densities or introduce many parameters. In addition, modelling the bias as a local parametric formula implies assuming the same galaxy formation physics everywhere in the Universe, and therefore the need of introducing complex models to account for different regimes, such as positive/negative threshold bias to boost/suppress galaxy formation. The hierarchical cosmic web approach addresses these issues by subdividing a tracer catalogue into subsets based on web environment (e.g. $4 \times 4 = 16$ regions in a two-level scheme), and applying a local parametric model in each subset. Each subset behaves like a separate tracer population, analogously to mass binning, but now organized by physically meaningful non-local information [10, 11]. In this way, the local bias model employed in each environment typically simplifies significantly, naturally accounting for the phenomena driving galaxy formation in each cosmic web environment. The spectral hierarchy generalizes the set of possible conditioning variables in a way that remains directly interpretable in bias-operator language.

6 Simulation Data

To investigate the spectral hierarchical cosmic web across a broad range of spatial scales, we analyse two complementary simulation datasets. A high-resolution particle-mesh simulation is used to explore the morphological structure of the hierarchy in the matter field, while a large-volume N -body simulation provides halo catalogues suitable for statistical tests of the information content relevant for large-scale structure analyses and mock generation.

6.1 High-resolution particle-mesh simulation

We first analyse a particle-mesh simulation designed to resolve the detailed morphology of the cosmic web hierarchy. The simulation volume has side length $L = 100 h^{-1}\text{Mpc}$ and contains 400^3 particles, corresponding to a spatial resolution $dL = 0.25 h^{-1}\text{Mpc}$.

The particle-mesh evolution is performed using the code FASTPM [46]. Initial conditions are generated using second-order Lagrangian perturbation theory (2LPT) at redshift $z = 99$ and evolved to $z = 1$ using 50 time steps. The force resolution is chosen to match the particle spacing. The density field is analysed on a cubic mesh with cell size $\Delta x = 0.25 h^{-1}\text{Mpc}$. The corresponding Nyquist frequency is $k_{\text{Nyquist}} \equiv (\pi/\Delta x) \simeq 12.5 h \text{Mpc}^{-1}$.

We construct the matter overdensity field $\delta(\mathbf{x})$ using a CIC mass-assignment scheme with tetrahedral tessellation [47]. All cosmic-web classification fields are evaluated on the same mesh.

This high-resolution setup allows us to investigate the detailed morphological behaviour of the spectral hierarchy in the matter field.

6.2 ABACUS dark matter and halo catalogues

To quantify the statistical information content of the hierarchy for biased tracers, we additionally analyse halo catalogues from the publicly available ABACUSSUMMIT simulation suite [48], produced with the ABACUS N -body code [49, 50].

The ABACUSSUMMIT simulations consist of 97 cosmological models centred around a base cosmology consistent with Planck 2018 [51]. Each simulation evolves 6912^3 particles in a volume of $(2h^{-1}\text{Gpc})^3$, corresponding to a particle mass of approximately $m_p \simeq 2 \times 10^9 h^{-1}M_\odot$, sufficient to resolve DESI-like tracers [52].

In this work we analyse one realisation of the base cosmology. We focus on $z=1.1$ for the information-content tests; the companion RLPT paper uses both $z=0.2$ and $z=1.1$ for gravity benchmarks. We use both the dark matter density field and the corresponding halo catalogue.

For the halo-based tests we select the most massive haloes until reaching a target number density of $n_h = 3 \times 10^{-3} (h \text{Mpc}^{-1})^3$, yielding approximately 8×10^6 haloes in the full simulation box. For the field-level analysis we work on a coarse cubic mesh with cell size $\Delta x \simeq 5.5 h^{-1}\text{Mpc}$, which matches the resolution regime typically used in fast large-volume forward modelling and mock production. The corresponding Nyquist frequency is $k_{\text{Nyquist}} \equiv (\pi/\Delta x) \simeq 0.57 h \text{Mpc}^{-1}$.

The halo overdensity field $\delta_h(\mathbf{x})$ is constructed using a nearest-grid-point assignment scheme. The matter field used for comparison is obtained by down-sampling the white-noise field of the corresponding ABACUS simulation to a mesh of 360^3 cells and evolving it with ALPT [53]. Cosmic-web classification fields are evaluated on the same mesh. The motivation for using ALPT in this second, low-resolution case is to investigate a practical and scalable setup in which the cross-correlation between the different cosmic-web regions is computed from a fast approximate gravity solver and compared directly to accurate tracer fields, here represented by the ABACUS halo catalogue, rather than relying on a down-sampled version of the expensive ABACUS dark matter field itself. This provides a realistic test of the regime relevant for mock production and field-level inference, where one typically has access to approximate dark matter realizations but wishes to recover the environmental information needed to model high-fidelity tracers. It also connects directly to the companion paper on ridged LPT, where we study subgrid modelling as a practical route to reconstruct the high-resolution halo distribution from low-resolution approximate gravity solvers.

7 Method: web classification, information-theoretic compression, and cross-correlation

In this section we describe how the spectral hierarchy is implemented in practice and how its information content is quantified. Our goal is to assess whether the categorical environmental information encoded at each hierarchy level i retains predictive power for halo clustering across Fourier scales relevant for fast mock production.

The procedure consists of three steps: (i) constructing generalized web classifications from the hierarchy tensors $\mathcal{H}_{ab}^{(i)}$, (ii) compressing the categorical web information into a four-value field that preserves the ordered morphology (void–sheet–filament–knot), and (iii) measuring the cross-correlation between this compressed web field and the halo overdensity field in Fourier space.

This pipeline allows us to test, in a controlled and information-theoretic way, whether the spectral hierarchy captures nontrivial halo-relevant structure from large scales down to the mesh Nyquist frequency.

7.1 Generalized eigenvalue web classification at level i

For each hierarchy level i , we compute $\delta^{(i)}$ via Eq. (2.10), construct $\mathcal{H}_{ab}^{(i)}$ via Eq. (2.12), and compute its ordered eigenvalues $\lambda_1^{(i)}$, $\lambda_2^{(i)}$, $\lambda_3^{(i)}$. We define web regions according to the number of eigenvalues exceeding a threshold $\lambda_{\text{th}}^{(i)}$. Assuming the ordering $\lambda_1^{(i)} \geq \lambda_2^{(i)} \geq \lambda_3^{(i)}$, the classification reads

- **knots:** $\lambda_3^{(i)} > \lambda_{\text{th}}^{(i)}$,
- **filaments:** $\lambda_2^{(i)} > \lambda_{\text{th}}^{(i)}$ and $\lambda_3^{(i)} \leq \lambda_{\text{th}}^{(i)}$,
- **sheets:** $\lambda_1^{(i)} > \lambda_{\text{th}}^{(i)}$ and $\lambda_2^{(i)} \leq \lambda_{\text{th}}^{(i)}$,
- **voids:** $\lambda_1^{(i)} \leq \lambda_{\text{th}}^{(i)}$,

[see 34, 36, 54, 55], By construction, these four classes are mutually exclusive and collectively exhaustive, so that every cell is assigned to exactly one web type. For the information-content demonstration below we focus on near-zero thresholds, with mild tuning only where needed to stabilize noise at high-derivative levels (as is standard in practical web classifiers).

To test whether the web hierarchy carries information relevant to halos across scales, we compress the web classification into a four-value field. Following hierarchical cosmic web work [11], we assign the ordered labels

$$w(\mathbf{x}) = \begin{cases} 4, & \text{knots,} \\ 3, & \text{filaments,} \\ 2, & \text{sheets,} \\ 1, & \text{voids,} \end{cases} \quad (7.1)$$

and define a corresponding web density contrast

$$\delta_{\text{web}}^{(i)}(\mathbf{x}) \equiv \frac{w^{(i)}(\mathbf{x})}{\langle w^{(i)} \rangle} - 1. \quad (7.2)$$

For Gaussian random fields, the joint distribution of the eigenvalues of the deformation tensor derived by Doroshkevich 1970 [25] implies that regions with one and two positive eigenvalues (sheet- and filament-like configurations) dominate the volume, while fully compressing or expanding configurations (knots and voids) are much less probable. The equidistant spacing adopted here should therefore not be interpreted as reflecting equal volume fractions, but rather as the simplest ordered encoding of the four web classes. This choice avoids introducing additional assumptions or optimization into the compression, and is sufficient for the present purpose of demonstrating that even a minimal categorical representation retains substantial cross-correlation with the tracer field. More general or optimized labelings could be explored in future work if required for specific practical applications.

8 Results: evidence for information in the hierarchy

In this section we investigate the behaviour of the spectral cosmic-web hierarchy in both simulations introduced above.

We first examine the qualitative morphology of the hierarchy using the high-resolution FASTPM simulation. This allows us to visualise how different hierarchy levels probe distinct spatial scales and geometric features of the matter field.

We then quantify the statistical information content of the hierarchy using the large-volume ABACUS simulation by measuring cross-correlations between the web-compressed fields and the halo density field.

8.1 Visual impression of hierarchical information

Figure 2 illustrates the behaviour of the spectral hierarchy in the high-resolution FASTPM simulation.

The top left panel shows the underlying matter density field. The subsequent panels display cosmic web classifications obtained from different hierarchy levels. The top right panel corresponds to the $i = -4$ classification ($-k^{-4}$ kernel), which strongly weighs long-wavelength modes. As expected, this level highlights only very broad spatial modulations of the density field. Fine filamentary structure is largely suppressed, indicating that $i = -4$ primarily probes ultra-large-scale morphology.

The mid left panel shows the classical potential-based classification ($i = -2$), corresponding to the standard tidal-tensor cosmic web. This level recovers the familiar network of filaments and knots associated with anisotropic gravitational collapse. For the high-resolution case we apply a logarithmic transformation of the density field prior to the web classification in order to reduce the impact of strongly nonlinear density peaks.

The subsequent panels—mid right ($i = 0$), bottom left ($i = 2$), and bottom right ($i = 4$)—progressively highlight smaller-scale structure. At $i = 0$, curvature information sharpens ridge and peak morphology relative to the potential web. The $i = 2$ and $i = 4$ levels further enhance small-scale curvature, producing increasingly localized ridge and knot patterns.

This progression demonstrates the ladder structure of the hierarchy: as the kernel index i increases, sensitivity shifts systematically from large-scale tidal morphology to increasingly local curvature features of the density field.

8.2 Cross power spectrum analysis

To quantify the information carried by the different hierarchy levels, we compute the cross power spectrum between the compressed web fields $\delta_{\text{web}}^{(i)}$ and the underlying tracer field.

8.2.1 High-resolution matter field.

We first analyse the high-resolution FASTPM simulation, where the web hierarchy is evaluated directly on the matter density field at resolution $\Delta x = 0.25 h^{-1}\text{Mpc}$. The cross-correlation coefficient between the matter overdensity δ and the web-compressed fields $\delta_{\text{web}}^{(i)}$ reveals a clear scale-dependent hierarchy of information content.

At intermediate nonlinear scales around $k \sim 1 h \text{Mpc}^{-1}$, all hierarchy levels remain highly correlated with the matter field. The measured correlations are $C^{(-2)} \simeq 0.87$, $C^{(0)} \simeq 0.91$, $C^{(2)} \simeq 0.92$, and $C^{(4)} \simeq 0.87$. At smaller scales the hierarchy becomes increasingly important.

For example, at $k \sim 10 h \text{ Mpc}^{-1}$ the correlations are $C^{(-2)} \simeq 0.14$, $C^{(0)} \simeq 0.53$, $C^{(2)} \simeq 0.68$, and $C^{(4)} \simeq 0.58$.

Thus, while the classical tidal-tensor level ($i = -2$) rapidly loses predictive power at high k , the higher hierarchy levels retain substantial correlation with the matter field. Toward the ultraviolet end of the spectrum, and especially close to the mesh Nyquist frequency, the $i = 4$ level provides the strongest correlation, indicating that the highest-derivative hierarchy level captures the most localized morphological information in the density field. This behaviour demonstrates that higher levels of the spectral hierarchy capture small-scale curvature information that is absent in the traditional tidal classification.

8.2.2 Halo field on coarse meshes.

We perform an analogous analysis using the halo catalogue from the ABACUSSUMMIT simulation.

Although ABACUSSUMMIT is intrinsically a significantly higher-resolution N -body simulation than the FASTPM run used above, the halo field is intentionally analysed on a much coarser mesh in the present study. This choice reflects the resolution regime typical of fast forward models and mock-generation pipelines.

In this setup the higher hierarchy levels already dominate the information content at moderately nonlinear scales. The transition occurs around $k \gtrsim 0.27 h \text{ Mpc}^{-1}$. At $k \simeq 0.5 h \text{ Mpc}^{-1}$, the correlations with the halo field are $C^{(-2)} \simeq 0.22$, $C^{(0)} \simeq 0.52$, $C^{(2)} \simeq 0.64$, $C^{(4)} \simeq 0.64$.

Figure 4 summarizes the central quantitative result of this work. In the high-resolution FASTPM matter field (top panel), the higher hierarchy levels $i = 0, 2, 4$ overtake the classical tidal-web level $i = -2$ at $k \gtrsim 0.6 h \text{ Mpc}^{-1}$, showing that the additional derivative levels encode substantially more information in the nonlinear regime. At $k \simeq 1 h \text{ Mpc}^{-1}$ the correlations are already slightly higher for $i = 0$ and $i = 2$ than for $i = -2$, while at $k \simeq 10 h \text{ Mpc}^{-1}$ the gain becomes dramatic: $C^{(-2)} \simeq 0.14$, compared with $C^{(0)} \simeq 0.53$, $C^{(2)} \simeq 0.68$, and $C^{(4)} \simeq 0.58$. A similar trend is found in the ABACUS halo analysis on coarse meshes (bottom panel), where levels higher than $i = -2$ begin to dominate at $k \gtrsim 0.27 h \text{ Mpc}^{-1}$. At $k \simeq 0.5 h \text{ Mpc}^{-1}$ the classical tidal-web level yields only $C^{(-2)} \simeq 0.22$, whereas the higher levels reach $C^{(0)} \simeq 0.52$ and $C^{(2)} \simeq C^{(4)} \simeq 0.64$. This demonstrates that higher levels of the spectral hierarchy provide a major gain in information content toward nonlinear scales.

Together these results demonstrate that the spectral hierarchy systematically extends the range of scales over which cosmic-web information remains relevant. While the classical tidal web captures large-scale anisotropic collapse, the higher derivative levels encode additional small-scale structure that becomes increasingly important toward nonlinear regimes.

8.3 PDF characterization and tracer footprint

A complementary characterization of the halo distribution is provided by the probability distribution functions (PDFs) in the different cosmic web regions, shown in Fig. 5. For simplicity and visual clarity, we restrict the binning to intervals of width 0.2 in the range $[0, 1]$. Considering four hierarchy levels from $i = -2$ to $i = 4$, each with four morphological classes, one obtains $4^4 = 256$ distinct cosmic web regions.

The resulting PDFs can be interpreted as the environmental footprint of the tracer population. Each tracer type populates the 256 regions with a characteristic distribution, encoding its response to long-range tidal structure, curvature, and higher-derivative local

environment. Rather than expanding in a large number of explicit nonlocal operators, one may describe tracers through their empirical footprint across hierarchy levels.

In this sense, the spectral hierarchy provides a compact and physically interpretable basis for tracer characterization. It compresses multi-scale environmental information into a discrete, low-dimensional structure that nevertheless retains substantial correlation with the halo density field across Fourier scales.

In Figs. 6 and 7 we illustrate how progressively more small-scale clustering information can be recovered by weighting the ALPT dark matter particles according to the halo number densities measured in the ABACUS simulation within increasingly refined cosmic-web partitions, namely 4, 16, 64, and 256 regions. Figure 6 shows this visually in a $250 h^{-1}\text{Mpc}$ subvolume: as the spectral hierarchy is refined, the weighted ALPT particle distribution increasingly resembles the spatial footprint of the halo field. The same trend is quantified in Fig. 7, where the high- k power spectrum converges toward the ABACUS halo clustering to within a few percent as more web regions are included. By contrast, the discrepancies at low k remain substantial, since in this exercise we only reweight the dark matter particles using halo number densities in web environments, without yet modelling the tracer number counts themselves. Those large-scale amplitudes would need to be supplied by an effective field-level bias model, whereas the present test isolates the gain in subgrid and small-scale information provided by the spectral cosmic-web hierarchy [56, for an extension of this exercise see the companion paper].

8.4 Implications for fast mock generation

The key practical implication is that the scale range over which the hierarchy retains information coincides with the resolution regime typical of large-volume fast lightcone simulations and mock pipelines. The spectral hierarchy therefore offers a viable environmental conditioning basis for fast mock generation: it captures information that would otherwise require either finer mesh resolution or more expensive dynamical modelling.

More broadly, this result supports the idea that cosmic web conditioning can serve as an efficient proxy for nonlocal bias operators, providing a computationally economical yet physically motivated route to incorporate environment-dependent effects in forward modelling and galaxy mock production. An application of this can be found in the subgrid modelling [see 12, 56].

9 Discussion and conclusions

We have introduced a spectral hierarchy of cosmic web classifications based on the kernel ladder $\delta^{(i)}(\mathbf{k}) \equiv -k^i \hat{\delta}(\mathbf{k})$ for even integer i . This construction unifies classical potential-based (tidal) and curvature-based web definitions, connects naturally to long- and short-range nonlocal bias operators, and extends the web concept to higher-derivative levels aligned with renormalised bias theory and EFT intuition.

The hierarchy provides a physically organized ladder of environmental descriptors. At the long-range end ($i = -4, -2$), the operators probe infrared structure and tidal anisotropy. At the intermediate level ($i = 0$), curvature and peak morphology become dominant. At higher levels ($i = 2, 4$), the hierarchy increasingly emphasizes short-range structure and higher-derivative operator content. This ordering is not merely formal: it manifests clearly both in configuration space (Fig. 3) and in Fourier space (Fig. 4), where the cross-correlation with halos shifts toward higher k for increasing i .

A central conceptual point, inspired by the hierarchical cosmic web assembly-bias framework [10, 11], is that cosmic web classification encodes the same tensor invariants that appear in nonlocal bias expansions. The ϕ -web ($i = -2$) implicitly conditions on (δ, s^2, s^3) through the invariants (I_1, I_2, I_3) , while the curvature web ($i = 0$) and higher-derivative levels ($i = 2, 4$) encode short-range operator content related to density-derivative tensors. The spectral hierarchy therefore provides a direct bridge between environmental segmentation and the operator language of perturbative bias.

An important practical advantage of the hierarchical web approach is that it avoids the pitfalls of explicitly truncated nonlocal bias expansions. Rather than introducing many operator terms with free coefficients, the tracer catalogue can be subdivided into web-conditioned subsets. Each subset behaves like a separate tracer population, analogous to mass binning but now organized by physically meaningful nonlocal information. Local positive-definite bias models can then be applied within each subset. This strategy naturally preserves positivity, limits parameter proliferation, and maintains interpretability [see 11, 57].

Our information-theoretic test demonstrates that even a highly compressed four-value web field retains significant correlation with the halo distribution from $k \sim 10^{-2} h \text{ Mpc}^{-1}$ up to the Nyquist scale of a $\Delta x \simeq 5.5 h^{-1} \text{ Mpc}$ mesh. The persistence of correlation at high k is particularly noteworthy, since the web field discards continuous density information and preserves only categorical morphology. The resulting 256-region PDF footprint (from four hierarchy levels) provides a compact tracer signature that may serve as a practical basis for bias learning and environmental characterization.

These findings have direct implications for fast mock galaxy catalogues. The relevant k -range coincides with the resolution regime typical of large-volume forward models and approximate gravity solvers. The spectral hierarchy therefore offers a computationally cheap yet physically grounded conditioning basis for mock generation. It can be used to learn bias relations from high-fidelity reference catalogues [e.g., 58] and transfer them to approximate solvers operating on coarse meshes, as in emerging bias-learning pipelines. Because the hierarchy is discrete and low-dimensional, it is inexpensive to compute and store on lightcones, and can be incorporated either in parametric region-wise fits or as structured features in controlled learning schemes.

Although the spectral hierarchy introduced here is not a fractal model, it is naturally related to fractal descriptions of large-scale structure in the sense that both characterize how morphology and clustering vary with scale. The present framework organizes this scale dependence through Fourier-space kernel weighting, whereas fractal approaches quantify it through real-space scaling exponents or dimensions. In approximately scale-free regimes, both descriptions are connected through the scaling relations between correlation functions and power spectra.

Beyond mock generation, the hierarchy provides a systematic framework for studying galaxy evolution and morphology–environment relations. By separating contributions from long-range tidal structure ($i = -2$), curvature and peak morphology ($i = 0$), and higher-derivative local environment ($i = 2, 4$), it becomes possible to disentangle environmental effects across physical scales. This scale-organized environmental basis may prove useful for investigating assembly bias, spin alignment, and morphology-dependent clustering [see, e.g., 59, 60]. This can be especially relevant in field-level inference [see 61].

The spectral hierarchy can be extended in several directions. Possible developments include:

- exploring the spectral hierarchy as a halo-identification framework beyond simple den-

sity maxima, complementing traditional density-based halo finders such as AMIGA HALO FINDER [62] and similar algorithms, by identifying relaxed structures through their multi-scale curvature and higher-derivative signatures;

- incorporating velocity-shear analogues and connections to velocity bias, since velocity-field web classifications encode information related to the velocity divergence θ (with $\theta \simeq \delta$ at linear order), and have been shown to help capture halo bias information toward smaller scales [see e.g. 10];
- optimizing eigenvalue thresholds $\lambda_{\text{th}}^{(i)}$ using information criteria, thereby significantly reducing the arbitrariness in the choice of the threshold once one moves away from the commonly adopted $\lambda_{\text{th}} = 0$;
- integrating hierarchy levels as conditioning variables in large-scale hierarchical assembly-bias models;
- mapping alternative gravity models onto Λ CDM simulations [see 45];
- exploring multi-tracer applications in which different galaxy populations respond to different hierarchy levels, shedding light on the connection between cosmological large-scale structure and galaxy formation.

In summary, the spectral hierarchy provides both a conceptual unification of cosmic web classifiers and a practical environmental compression scheme. It organizes nonlocal information in a scale-ordered ladder, demonstrably retains halo-relevant information up to mesh Nyquist scales, and offers a structured, interpretable basis for next-generation mock generation and environmental studies of galaxy formation.

Acknowledgements

The authors thank the HOLI-mocks team for useful discussions and testing the WEBON-code, special mention to Ana Almeida, José María Coloma-Nadal, Ginevra Favole, Daniel Forero Sánchez, Jorge García Farieta, Fernando Frías García Lago, Pere Rosselló Truyols, Yunyi Tang, Natalia Villa Nova Rodrigues, Cheng Zhao. FSK acknowledges the Instituto de Astrofísica de Canarias (IAC) for continuous support to the *Cosmology with LSS probes* activities and the Spanish Ministry for Innovation and Science / Agencia Estatal de Investigación for support of the project *Big Data of the Cosmic Web* (PID2020-120612GB-I00/AEI/10.13039/501100011033), under which this work has been conceived and carried out, and the *FIRE (Field-level bayesian Inference to Reconstruct the univErse)* project, which has been recently funded by a *Proyecto de Generación de Conocimiento 2024*, PID2024-160504NB-I00. FS acknowledges support from the *Institute for Fundamental Physics of the Universe* postdoctoral fellowship scheme. FS is also grateful to IAC for hospitality during part of the realization of this project.

Disclaimer

The Web0n code used in this work has been mainly written by FSK in C++ without AI.

Web0n is a modular framework whose methodological components are presented across three companion papers: the present work on the spectral hierarchical cosmic-web classification; a dedicated paper on ridged Lagrangian perturbation theory [56]; a further paper

describing the lightcone evolution mode within the HOLI-mocks pipeline to produce the DESI covariance mocks used for the DR2 Key Projects [63] (see: www.cosmic-signal.org). WebOn has already been used in three previous publications: one presenting the *Hierarchical cosmic web and assembly bias* [11] approach for effective field-level bias modelling exploiting the hierarchical cosmic web k^{-2} and k^0 levels; one presenting *Cosmomia: cosmic-web based redshift-space halo distribution* [12] for subgrid modelling exploiting the knots k^0 level as attractors; and *Fast and accurate Gaia-unWISE quasar mock catalogs from LPT and Eulerian bias* [64], using the two-hundred $10 h^{-1}$ Gpc side cubical volume simulations performed with the lightcone evolution WEBON code on the Leonardo@CINECA pre-exascale supercomputing facilities in September 2023 through the INAF_C9A09 HPC proposal (637k core hrs). It has also served as a reference for its JaX differentiable version in *Differentiable Fuzzy Cosmic-Web for Field Level Inference* [61], which is under active development.

References

- [1] R. van de Weygaert and J.R. Bond, *Clusters and the Theory of the Cosmic Web*, in *A Pan-Chromatic View of Clusters of Galaxies and the Large-Scale Structure*, M. Plionis, O. López-Cruz and D. Hughes, eds., vol. 740, p. 335 (2008), DOI.
- [2] R. van de Weygaert and W. Schaap, *The Cosmic Web: Geometric Analysis*, in *Data Analysis in Cosmology*, V.J. Martínez, E. Saar, E. Martínez-González and M.J. Pons-Bordería, eds., vol. 665, pp. 291–413 (2009), DOI.
- [3] N.I. Libeskind, R. van de Weygaert, M. Cautun, B. Falck, E. Tempel, T. Abel et al., *Tracing the cosmic web*, *MNRAS* **473** (2018) 1195 [1705.03021].
- [4] D. Eckert, M. Jauzac, H. Shan, J.-P. Kneib, T. Erben, H. Israel et al., *Warm-hot baryons comprise 5-10 per cent of filaments in the cosmic web*, *Nature* **528** (2015) 105 [1512.00454].
- [5] F.-S. Kitaura, C.-H. Chuang, Y. Liang, C. Zhao, C. Tao, S. Rodríguez-Torres et al., *Signatures of the Primordial Universe from Its Emptiness: Measurement of Baryon Acoustic Oscillations from Minima of the Density Field*, *Phys. Rev. Lett.* **116** (2016) 171301 [1511.04405].
- [6] C.-H. Chuang, F.-S. Kitaura, Y. Liang, A. Font-Ribera, C. Zhao, P. McDonald et al., *Linear redshift space distortions for cosmic voids based on galaxies in redshift space*, *Phys. Rev. D* **95** (2017) 063528 [1605.05352].
- [7] A. Kovács, C. Sánchez, J. García-Bellido, J. Elvin-Poole, N. Hamaus, V. Miranda et al., *More out of less: an excess integrated Sachs-Wolfe signal from supervoids mapped out by the Dark Energy Survey*, *MNRAS* **484** (2019) 5267 [1811.07812].
- [8] P. McDonald and A. Roy, *Clustering of dark matter tracers: generalizing bias for the coming era of precision LSS*, *J. Cosmology Astropart. Phys.* **2009** (2009) 020 [0902.0991].
- [9] V. Desjacques, D. Jeong and F. Schmidt, *Large-scale galaxy bias*, *Phys. Rep.* **733** (2018) 1 [1611.09787].
- [10] F.S. Kitaura, A. Balaguera-Antolínez, F. Sinigaglia and M. Pellejero-Ibáñez, *The cosmic web connection to the dark matter halo distribution through gravity*, *MNRAS* **512** (2022) 2245 [2005.11598].
- [11] J.M. Coloma-Nadal, F.S. Kitaura, J.E. García-Farieta, F. Sinigaglia, G. Favole and D. Forero Sánchez, *The Hierarchical Cosmic Web and Assembly Bias*, *arXiv e-prints* (2024) arXiv:2403.19337 [2403.19337].
- [12] D. Forero-Sánchez, F.-S. Kitaura, F. Sinigaglia, J. María Coloma-Nodal and J.-P. Kneib, *CosmoMIA: Cosmic Web-based redshift space halo distribution*, *arXiv e-prints* (2024) arXiv:2402.17581 [2402.17581].

- [13] O. Hahn, C. Porciani, C.M. Carollo and A. Dekel, *Properties of dark matter haloes in clusters, filaments, sheets and voids*, *MNRAS* **375** (2007) 489 [[astro-ph/0610280](#)].
- [14] O. Hahn and A. Paranjape, *General relativistic screening in cosmological simulations*, *Phys. Rev. D* **94** (2016) 083511 [[1602.07699](#)].
- [15] F. Bernardeau, S. Colombi, E. Gaztañaga and R. Scoccimarro, *Large-scale structure of the universe and cosmological perturbation theory*, *Physics Reports* **367** (2002) 1.
- [16] N.E. Chisari and M. Zaldarriaga, *Connection between Newtonian simulations and general relativity*, *Phys. Rev. D* **83** (2011) 123505 [[1101.3555](#)].
- [17] T. Baldauf, U. Seljak, L. Senatore and M. Zaldarriaga, *Galaxy bias and non-linear structure formation in general relativity*, *J. Cosmology Astropart. Phys.* **2011** (2011) 031 [[1106.5507](#)].
- [18] J. Adamek, D. Daverio, R. Durrer and M. Kunz, *General relativistic N-body simulations in the weak field limit*, *Phys. Rev. D* **88** (2013) 103527 [[1308.6524](#)].
- [19] J. Adamek, D. Daverio, R. Durrer and M. Kunz, *General relativity and cosmic structure formation*, *Nature Physics* **12** (2016) 346 [[1509.01699](#)].
- [20] N. Dalal, O. Doré, D. Huterer and A. Shirokov, *Imprints of primordial non-gaussianities on large-scale structure: Scale-dependent bias and abundance of virialized objects*, *Phys. Rev. D* **77** (2008) 123514.
- [21] R. Martinez-Carrillo, J.C. Hidalgo, K.A. Malik and A. Pourtsidou, *Contributions from primordial non-Gaussianity and general relativity to the galaxy power spectrum*, *J. Cosmology Astropart. Phys.* **2021** (2021) 025 [[2107.10815](#)].
- [22] V. Assassi, D. Baumann and F. Schmidt, *Galaxy bias and primordial non-Gaussianity*, *J. Cosmology Astropart. Phys.* **2015** (2015) 043 [[1510.03723](#)].
- [23] M. Bruni, R. Crittenden, K. Koyama, R. Maartens, C. Pitrou and D. Wands, *Disentangling non-Gaussianity, bias, and general relativistic effects in the galaxy distribution*, *Phys. Rev. D* **85** (2012) 041301 [[1106.3999](#)].
- [24] P.J.E. Peebles, *Origin of the angular momentum of galaxies*, *ApJ* **155** (1969) 393.
- [25] A.G. Doroshkevich, *The space structure of perturbations and the origin of rotation of galaxies in the theory of fluctuation.*, *Astrofizika* **6** (1970) 581.
- [26] P. Catelan and T. Theuns, *Evolution of the angular momentum of protogalaxies*, *MNRAS* **282** (1996) 436.
- [27] A. Heavens and J. Peacock, *Tidal torques and local density maxima*, *Monthly Notices of the Royal Astronomical Society* **232** (1988) 339.
- [28] C. Porciani, A. Dekel and Y. Hoffman, *Testing tidal-torque theory - i*, *MNRAS* **332** (2002) 325.
- [29] C. Porciani, A. Dekel and Y. Hoffman, *Testing tidal-torque theory - ii*, *MNRAS* **332** (2002) 339.
- [30] J.M. Bardeen, J.R. Bond, N. Kaiser and A.S. Szalay, *The statistics of peaks of gaussian random fields*, *ApJ* **304** (1986) 15.
- [31] V. Desjacques, *Environmental dependence of halo formation*, *Phys. Rev. D* **82** (2010) 103503 [[1006.0007](#)].
- [32] F. Sinigaglia, F.-S. Kitaura, A. Balaguera-Antolínez, K. Nagamine, M. Ata, I. Shimizu et al., *The bias from hydrodynamic simulations: Mapping baryon physics onto dark matter fields*, *The Astrophysical Journal* **921** (2021) 66.
- [33] N. Dalal, M. White, J.R. Bond and A. Shirokov, *Halo Assembly Bias in Hierarchical Structure Formation*, *ApJ* **687** (2008) 12 [[0803.3453](#)].
- [34] Y.B. Zel'dovich, *Gravitational instability: An approximate theory for large density perturbations.*, *A&A* **5** (1970) 84.

- [35] S.D.M. White, *Angular momentum growth in protogalaxies*, *ApJ* **286** (1984) 38.
- [36] O. Hahn, C. Porciani, C.M. Carollo and A. Dekel, *Properties of dark matter haloes in clusters, filaments, sheets and voids*, *Monthly Notices of the Royal Astronomical Society* **375** (2007) 489.
- [37] J. Lesgourgues and S. Pastor, *Massive neutrinos and cosmology*, *Phys. Rep.* **429** (2006) 307 [[astro-ph/0603494](#)].
- [38] J.J.M. Carrasco, M.P. Hertzberg and L. Senatore, *The effective field theory of cosmological large scale structures*, *Journal of High Energy Physics* **2012** (2012) 82 [[1206.2926](#)].
- [39] E. Pajer and M. Zaldarriaga, *On the renormalization of the effective field theory of large scale structures*, *J. Cosmology Astropart. Phys.* **2013** (2013) 037 [[1301.7182](#)].
- [40] L. Senatore and M. Zaldarriaga, *The IR-resummed Effective Field Theory of Large Scale Structures*, *J. Cosmology Astropart. Phys.* **2015** (2015) 013 [[1404.5954](#)].
- [41] L. Senatore, *Bias in the effective field theory of large scale structures*, *J. Cosmology Astropart. Phys.* **2015** (2015) 007 [[1406.7843](#)].
- [42] S. Tsujikawa, *Matter density perturbations and effective gravitational constant in modified gravity models of dark energy*, *Phys. Rev. D* **76** (2007) 023514 [[0705.1032](#)].
- [43] A. De Felice and S. Tsujikawa, *$f(r)$ theories*, *Living Reviews in Relativity* **13** (2010) 3 [[1002.4928](#)].
- [44] W. Hu, R. Barkana and A. Gruzinov, *Fuzzy Cold Dark Matter: The Wave Properties of Ultralight Particles*, *Phys. Rev. Lett.* **85** (2000) 1158 [[astro-ph/0003365](#)].
- [45] J.E. García-Farieta, A. Balaguera-Antolínez and F.-S. Kitaura, *Fast simulation mapping: From standard to modified gravity cosmologies using the bias assignment method*, *A&A* **690** (2024) A27 [[2405.10319](#)].
- [46] Y. Feng, M.-Y. Chu, U. Seljak and P. McDonald, *FASTPM: a new scheme for fast simulations of dark matter and haloes*, *MNRAS* **463** (2016) 2273 [[1603.00476](#)].
- [47] T. Abel, O. Hahn and R. Kaehler, *Tracing the dark matter sheet in phase space*, *Monthly Notices of the Royal Astronomical Society* **427** (2012) 61 [[1111.3944](#)].
- [48] N.A. Maksimova, L.H. Garrison, D.J. Eisenstein, B. Hadzhiyska, S. Bose and T.P. Satterthwaite, *ABACUSSUMMIT: a massive set of high-accuracy, high-resolution N-body simulations*, *MNRAS* **508** (2021) 4017 [[2110.11398](#)].
- [49] L.H. Garrison, D.J. Eisenstein, D. Ferrer, J.L. Tinker, P.A. Pinto and D.H. Weinberg, *The Abacus Cosmos: A Suite of Cosmological N-body Simulations*, *ApJS* **236** (2018) 43 [[1712.05768](#)].
- [50] L.H. Garrison, D.J. Eisenstein, D. Ferrer, N.A. Maksimova and P.A. Pinto, *The ABACUS cosmological N-body code*, *MNRAS* **508** (2021) 575 [[2110.11392](#)].
- [51] Planck Collaboration, N. Aghanim, Y. Akrami, M. Ashdown, J. Aumont, C. Baccigalupi et al., *Planck 2018 results. VI. Cosmological parameters*, *A&A* **641** (2020) A6 [[1807.06209](#)].
- [52] M. Levi, L.E. Allen, A. Raichoor, C. Baltay, S. BenZvi, F. Beutler et al., *The Dark Energy Spectroscopic Instrument (DESI)*, in *Bulletin of the American Astronomical Society*, vol. 51, p. 57, Sept., 2019, DOI [[1907.10688](#)].
- [53] F.-S. Kitaura and S. Heß, *Cosmological structure formation with augmented lagrangian perturbation theory*, *Monthly Notices of the Royal Astronomical Society: Letters* **435** (2013) L78.
- [54] J.R. Bond, L. Kofman and D. Pogosyan, *How filaments of galaxies are woven into the cosmic web*, *Nature* **380** (1996) 603 [[astro-ph/9512141](#)].

- [55] J.E. Forero–Romero, Y. Hoffman, S. Gottlöber, A. Klypin and G. Yepes, *A dynamical classification of the cosmic web*, *Monthly Notices of the Royal Astronomical Society* **396** (2009) 1815 [<https://academic.oup.com/mnras/article-pdf/396/3/1815/5804803/mnras0396-1815.pdf>].
- [56] F.-S. Kitaura, F. Sinigaglia, et al., *in preparation* (2026) .
- [57] F. Sinigaglia, F.S. Kitaura, K. Nagamine, Y. Oku and A. Balaguera-Antolínez, *Field-level Lyman- α forest modeling in redshift space via augmented nonlocal Fluctuating Gunn-Peterson Approximation*, *A&A* **682** (2024) A21 [2305.10428].
- [58] G. Favole, F.-S. Kitaura, B. Hadzhiyska, D.J. Eisenstein, L.H. Garrison and S. Bose, *ELG \times LRG distribution through dark matter halo dynamics*, *arXiv e-prints* (2025) arXiv:2512.04362 [2512.04362].
- [59] S.E. Nuza, F.-S. Kitaura, S. Heß, N.I. Libeskind and V. Müller, *The cosmic web of the Local Universe: cosmic variance, matter content and its relation to galaxy morphology*, *MNRAS* **445** (2014) 988 [1406.1004].
- [60] A. Paranjape, O. Hahn and R.K. Sheth, *Halo assembly bias and the tidal anisotropy of the local halo environment*, *MNRAS* **476** (2018) 3631 [1706.09906].
- [61] P. Rosselló, F.-S. Kitaura, D. Forero-Sánchez, F. Sinigaglia and G. Favole, *Differentiable Fuzzy Cosmic-Web for Field Level Inference*, *arXiv e-prints* (2025) arXiv:2506.03969 [2506.03969].
- [62] S.R. Knollmann and A. Knebe, *AHF: Amiga’s Halo Finder*, *ApJS* **182** (2009) 608 [0904.3662].
- [63] F.-S. Kitaura, F. Sinigaglia, et al., *in preparation* (2026) .
- [64] F. Sinigaglia, F.-S. Kitaura, M. Shiferaw, G. Favole, K. Storey-Fisher and N. Arsenov, *Fast and accurate Gaia-unWISE quasar mock catalogs from LPT and Eulerian bias*, *arXiv e-prints* (2025) arXiv:2509.15890 [2509.15890].

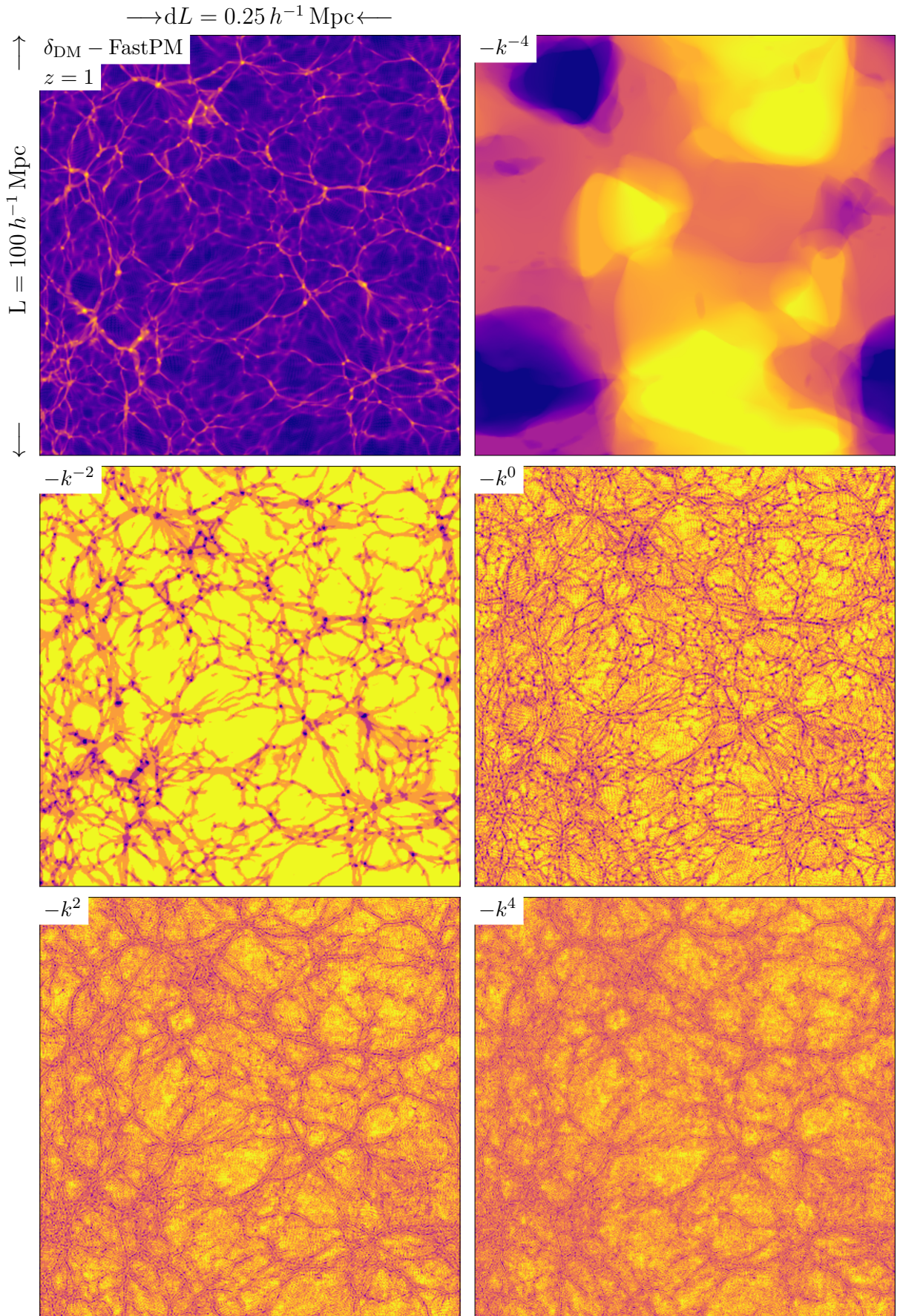


Figure 2. Top left: FASTPM at $z = 1$ assigned to a mesh. The side length is $100 h^{-1} \text{Mpc}$ and the cell size is $dL \simeq 0.25 h^{-1} \text{Mpc}$. Other panels show the cosmic web classification contrast corresponding to the kernel hierarchy: (top right) $-k^{-4}$, (middle left) $-k^{-2}$, (middle right) $-k^0$, (bottom left) $-k^2$, (bottom right) $-k^4$.

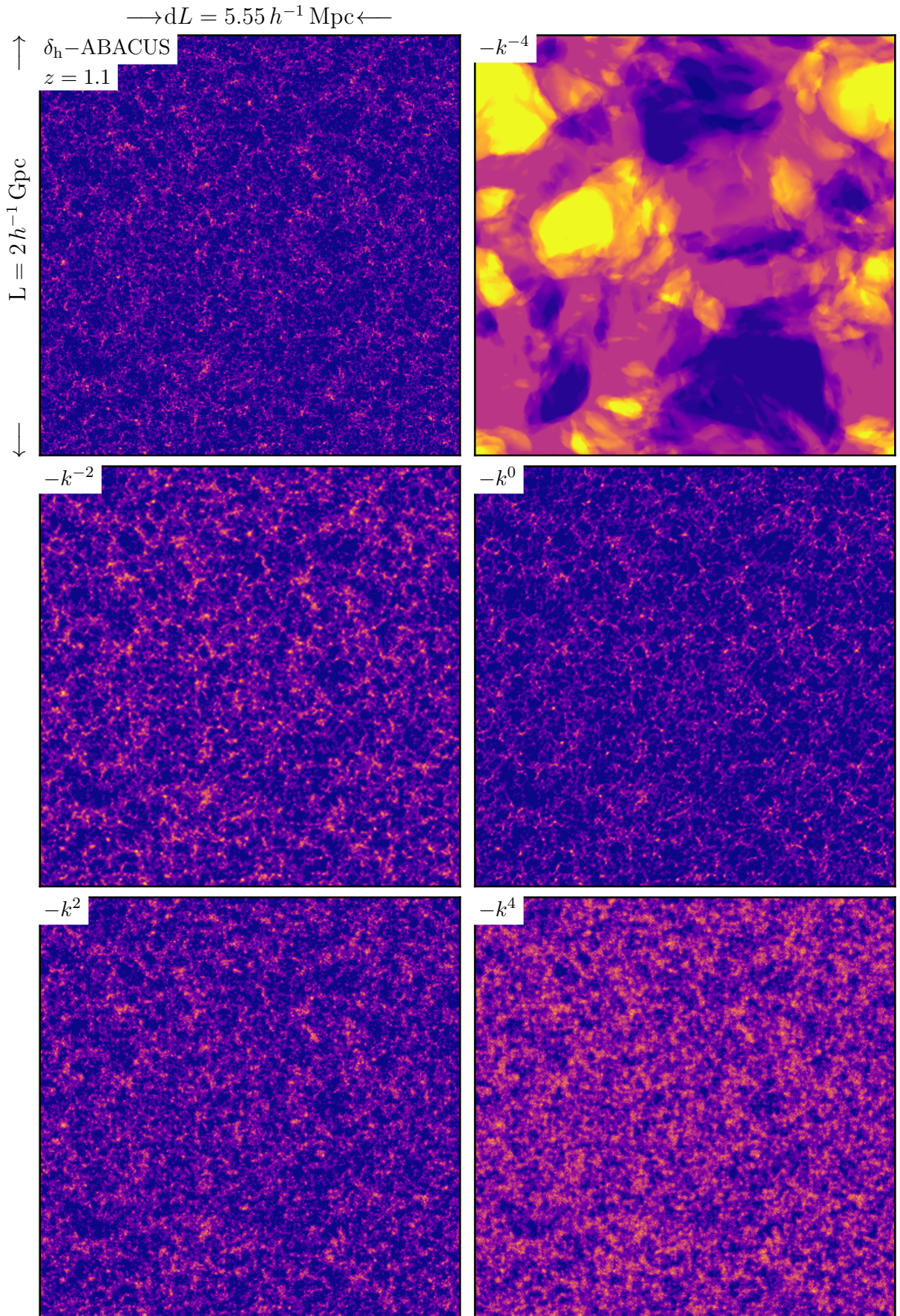


Figure 3. Top left: ABACUS “000” distinct halos at $z = 1.1$ assigned to a mesh. The side length is $2000 h^{-1} \text{Mpc}$ and the cell size is $dL \simeq 5.55 h^{-1} \text{Mpc}$. Other panels show the cosmic web classification contrast corresponding to the kernel hierarchy: (top right) $-k^{-4}$, (middle left) $-k^{-2}$, (middle right) $-k^0$, (bottom left) $-k^2$, (bottom right) $-k^4$.

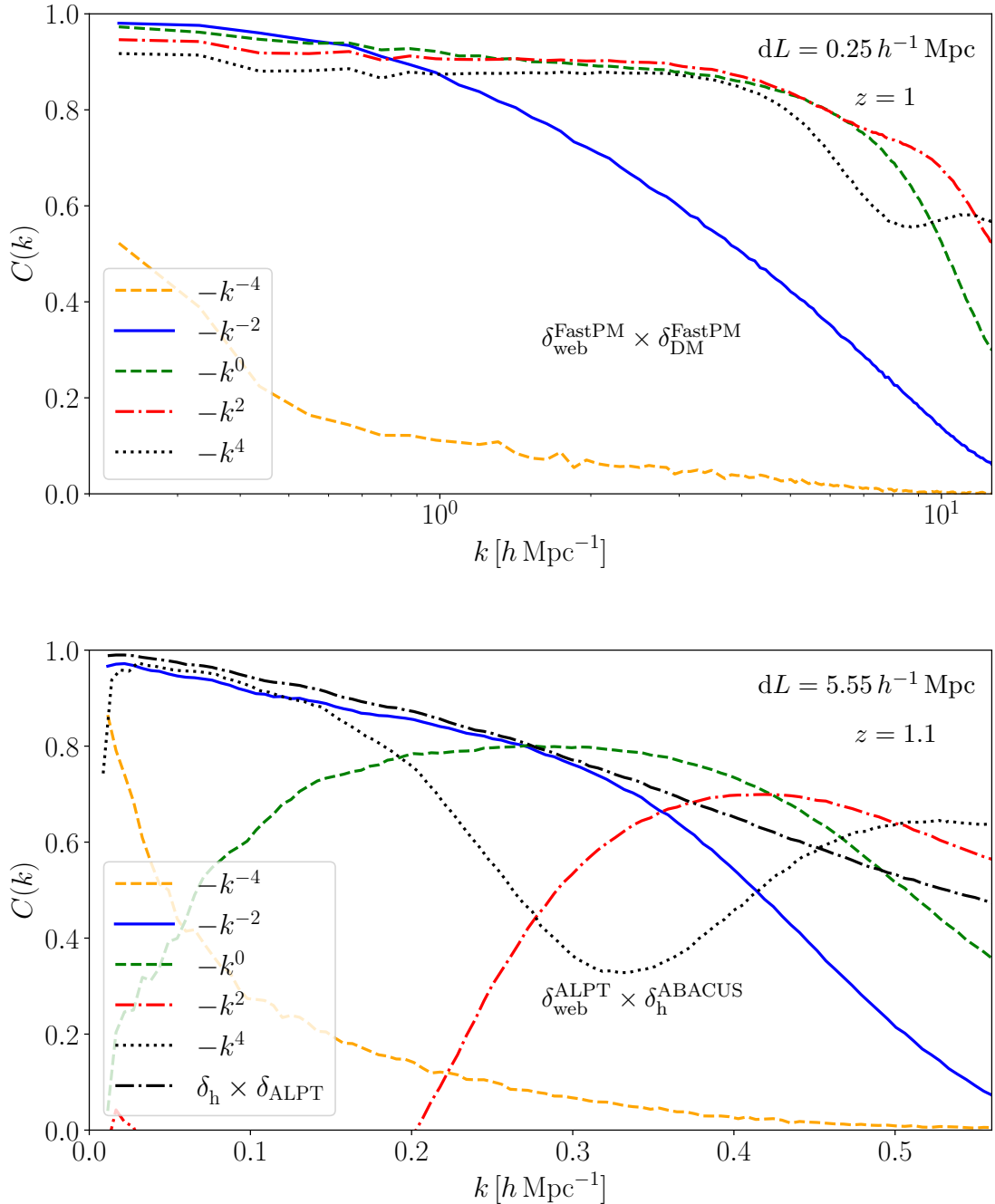


Figure 4. Cross-correlation coefficient $C^{(i)}(k)$ for the different hierarchy levels $i = -4, -2, 0, 2, 4$. The coefficient is defined as $C^{(i)}(k) = \langle \hat{\delta}_{\text{tr}}^*(\mathbf{k}) \hat{\delta}_{\text{web}}^{(i)}(\mathbf{k}) \rangle / \sqrt{P_{\text{tr}}(k) P_{\text{web}}^{(i)}(k)}$, where δ_{tr} denotes the tracer field and $\delta_{\text{web}}^{(i)}$ the compressed web-density-contrast field at hierarchy level i . **Top panel:** high-resolution FASTPM matter field at $z = 1$ with mesh spacing $dL = 0.25 h^{-1} \text{ Mpc}$. **Bottom panel:** ABACUSSUMMIT halo field at $z = 1.1$, analysed on a coarse mesh with $dL = 5.55 h^{-1} \text{ Mpc}$; the corresponding web fields are computed from an ALPT matter field generated from the down-sampled initial conditions of the same simulation. The threshold is set to $\lambda_{\text{th}}^{(i)} = 0$ for all hierarchy levels except $i = 4$, where a small stabilizing threshold $\lambda_{\text{th}}^{(4)} = 0.001$ is adopted. The figure shows that the classical tidal-web level $i = -2$ dominates on large scales, whereas the higher hierarchy levels $i = 0, 2, 4$ retain significantly more information toward nonlinear scales, both in the high-resolution matter field and in the coarse-mesh halo analysis.

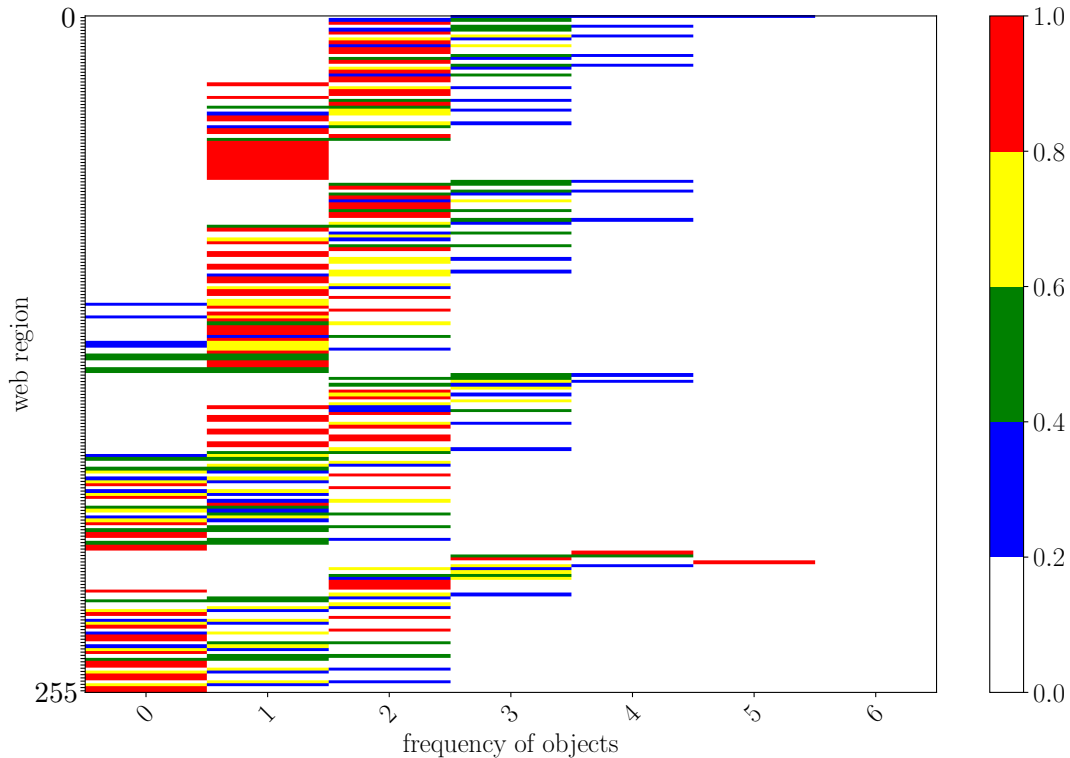


Figure 5. Environmental footprint of the halo population across the spectral hierarchy. The figure shows the probability distribution functions (PDFs) of halo occupation within the 256 cosmic web regions obtained from four hierarchy levels ($i = -2, 0, 2, 4$), each subdivided into four morphological classes (voids, sheets, filaments, knots). For clarity, the PDF values are binned in intervals of width 0.2 in the range $[0, 1]$. Each bin corresponds to a distinct combination of web classifications across levels, forming a discrete multi-scale environmental signature of the tracer population. The non-uniform occupation across regions demonstrates that halos respond differently to long-range tidal structure, curvature, and higher-derivative local environment. This multi-level PDF can therefore be interpreted as the environmental footprint of the tracer population and provides a compact basis for bias characterization and environmental modelling.

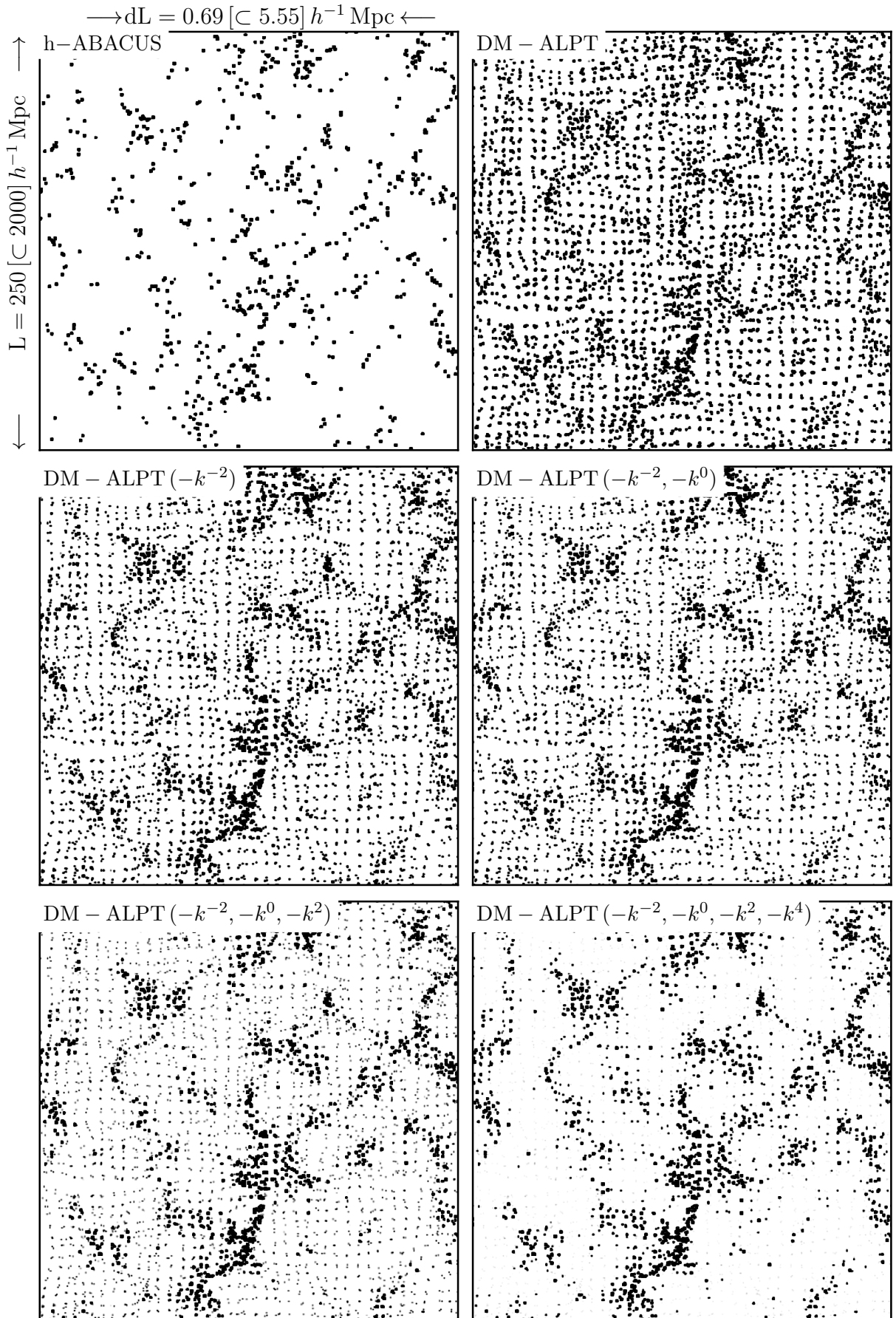


Figure 6. Slice of a $250 h^{-1}\text{Mpc}$ subvolume extracted from the ABACUS simulation, represented on a 360^3 mesh with cell size $dL = 0.69, h^{-1}\text{Mpc}$. The **upper panels** show the ABACUS halo number counts (**left**), and the ALPT dark matter particle positions on the high resolution mesh (**right**). The **remaining panels** display the dark matter particles after assigning masses according to halo number densities measured in the ABACUS simulation for different cosmic-web regions defined by the spectral hierarchy computed from the ALPT field (see text for details).

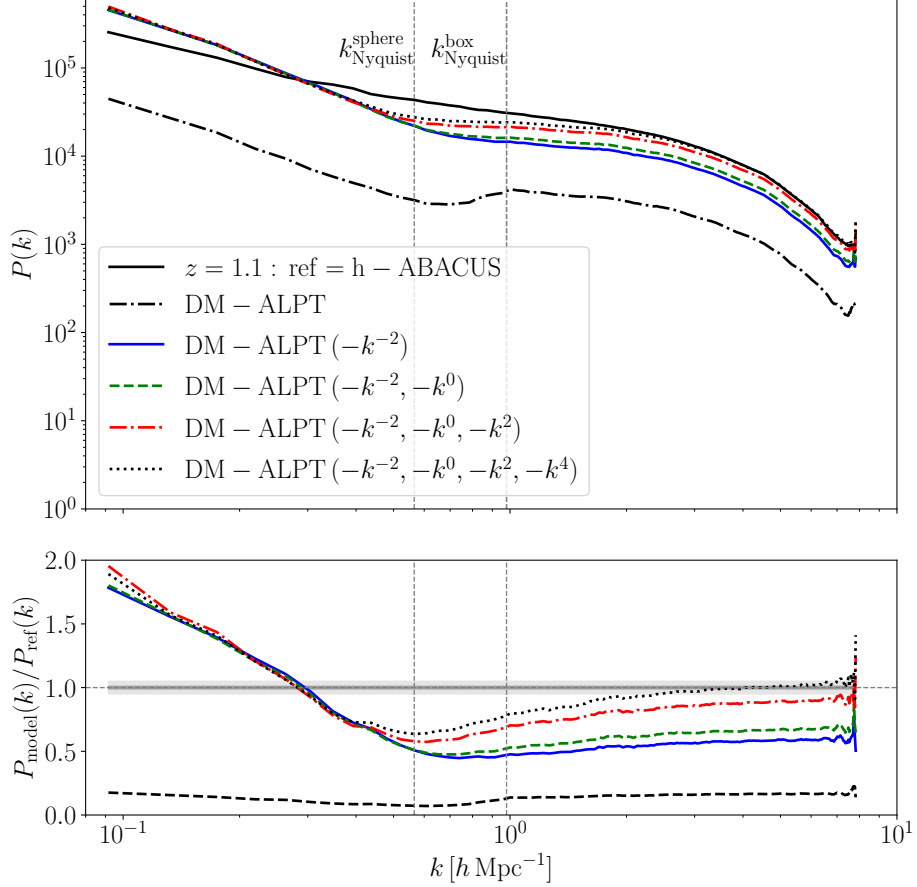


Figure 7. Power spectra of the different halo and dark matter fields. The solid line shows the halo distribution from the ABACUS simulation on a mesh with resolution $dL = 0.69, h^{-1}\text{Mpc}$. The dash-dotted line corresponds to the ALPT dark matter particle distribution from the low-resolution mesh gridded onto the high-resolution mesh. The subsequent DM-ALPT curves represent the same dark matter field constrained to match the ABACUS halo number densities in progressively finer cosmic-web hierarchies. The box Nyquist frequency is $k_{\text{Nyquist}}^{\text{box}} = k_{\text{Nyquist}}^{\text{sphere}} \times \sqrt{3} \simeq 0.99$.